BIOENGINEERING

Injectable hydrogel with MSNs/microRNA-21-5p delivery enables both immunomodification and enhanced angiogenesis for myocardial infarction therapy in pigs

Yan Li[1,2]*, Xin Chen[3]*, Ronghua Jin[3], Lu Chen[1], Ming Dang[4], Hao Cao[5], Yun Dong[5], Bolei Cai[2], Guo Bai[1], J. Justin Gooding[6], Shiyu Liu[7], Duohong Zou[1†], Zhiyuan Zhang[1†], Chi Yang[1†]

Current therapeutic strategies such as angiogenic therapy and anti-inflammatory therapy for treating myocardial infarction have limited success. An effective approach may benefit from resolution of excessive inflammation combined with enhancement of angiogenesis. Here, we developed a microRNA-21-5p delivery system using functionalized mesoporous silica nanoparticles (MSNs) with additional intrinsic therapeutic effects. These nanocarriers were encapsulated into an injectable hydrogel matrix (Gel@MSN/miR-21-5p) to enable controlled on-demand microRNA-21 delivery triggered by the local acidic microenvironment. In a porcine model of myocardial infarction, we demonstrated that the released MSN complexes notably inhibited the inflammatory response by inhibiting the polarization of M1 macrophage within the infarcted myocardium, while further microRNA-21-5p delivery by MSNs to endothelial cells markedly promoted local neovascularization and rescued at-risk cardiomyocytes. The synergy of anti-inflammatory and proangiogenic effects effectively reduced infarct size in a porcine model of myocardial infarction.

INTRODUCTION

Myocardial infarction (MI) remains one of the leading causes of death worldwide. The inflammatory response caused by MI sets the stage for fibrous tissue and often progresses to chronic heart failure (1), resulting in a more than 50% 5-year mortality after MI (2). An immunomodulation strategy, which prevents an excessive inflammatory response, can be beneficial to reduce scar tissue formation. Immunomodulation alone can likely prevent ongoing damage but fails to restore the compromised heart function. Promoting angiogenesis in the infarct area has the potential to reperfuse and salvage the surviving ischemic myocardium (3). Therefore, we hypothesize that long-term improvements in heart function after MI can be achieved by the combination of resolving inflammation and promoting angiogenesis in the infarct area.

Various therapeutics, such as cell transplant, exosomes, and nucleic acids, have been explored to treat MI and restore cardiac function, with varying degrees of success. Cell transplantation could enhance the functions of the infarcted heart (4), but only cardiomyocytes derived from pluripotent stem cells have been shown to engraft and generate functional myocardium (5). Limitations in cell sources, potential immune responses, and rigorous regulations hinder the clinical translation of cell-based therapies. Several studies have shown that cell-derived exosomes may be effective in treating cardiovascular diseases (6). However, there are obvious variations in exosomes resulting from multiple factors such as cell phenotype, preparation procedure, and exosome storage conditions (7). MicroRNAs (miRNA) are appealing genetic tools to stimulate cardiac performance, as they could regulate the levels of multiple genes simultaneously. Recently, it has been suggested that the cardiovascular system is regulated via a miRNA network (8). High-throughput screening work revealed that miRNAs, particularly microRNA-21-5p (miR-21-5p), are highly expressed in endothelial cells and stimulate angiogenesis by targeting antiangiogenic genes (9). miRNAs have a unique capacity to simultaneously promote the secretion of multiple endogenous molecules that might enhance vessel regeneration in the ischemic tissue. Negatively charged miRNAs typically cannot cross the cell membrane without a transfection agent. In addition, miRNAs are relatively unstable and can be degraded rapidly in vivo (10). Thus, vectors that protect and deliver miRNAs into cells are crucial to improve the efficacy of miRNA therapy.

Mesoporous silica nanoparticles (MSNs) have been developed as a promising vector for miRNA delivery because of their many excellent properties, such as good biocompatibility and high transfection efficiency. Moreover, studies have shown that inflammation can be modulated by phagocytosis of micro/nanomaterials, such as liposomes (11), polymer particles (12, 13), and inorganic particles (14). Macrophages play a central role in regulating infarct-induced inflammation because they adopt proinflammatory (M1) phenotypes. In this study, we found that MSNs showed great potential in inhibiting

[1]National Clinical Research Center for Oral Diseases; Shanghai Key Laboratory of Stomatology and Shanghai Research Institute of Stomatology, Department of Oral Surgery, Shanghai Ninth People's Hospital, College of Stomatology, Shanghai Jiao Tong University School of Medicine, Shanghai 200011, China. [2]State Key Laboratory of Military Stomatology and National Clinical Research Center for Oral Diseases and Shaanxi Key Laboratory of Oral Diseases, Department of Prosthodontics, School of Stomatology, The Fourth Military Medical University, Xi'an 710032, China. [3]School of Chemical Engineering and Technology, Shaanxi Key Laboratory of Energy Chemical Process Intensification, Institute of Polymer Science in Chemical Engineering, Xi'an Jiao Tong University, Xi'an 710049, China. [4]School of Dentistry, University of Michigan, Ann Arbor, MI 48109, USA. [5]Department of Cardiac Surgery, Shanghai East Hospital, Tongji University School of Medicine, Shanghai 200120, China. [6]School of Chemistry, Australian Centre for NanoMedicine and ARC Australian, Centre of Excellence in Convergent Bio-Nano Science and Technology, University of New South Wales, Sydney 2052, Australia. [7]Key Laboratory of Military Stomatology and National Clinical Research Center for Oral Diseases and Shaanxi Key Laboratory of Oral Diseases, Center for Tissue Engineering, School of Stomatology, The Fourth Military Medical University, Xi'an, Shaanxi 710032, China.
*These authors contributed equally to this work.
†Corresponding author. Email: yangchi63@hotmail.com (C.Y.); zhzhy0502@163.com (Z.Z.); zdhyy@ahmu.edu.cn (D.Z.)

M1 polarization following inflammation both in vitro and in vivo (see details in Results). Therefore, we engineered an MSN/miR-21-5p complex by combining MSN, a potential anti-inflammatory nanomaterial, and miR-21-5p, a proangiogenic therapeutic.

RNA interference (RNAi) is a promising therapeutic approach for various diseases (15). An important aspect in RNAi delivery system design is to ensure precise spatiotemporal release (16–21). Uncontrolled delivery of miRNA in the heart could result in sudden arrhythmia, as reported by Gabisonia et al. (22). In addition, studies have also identified that a big challenge for RNAi-based therapeutics is to achieve highly localized RNAi delivery (16, 18, 19, 23). Drug release from conventional hydrogels (24, 25) is controlled by passive diffusion and often results in off-target effects (26). In contrast, MSN/miR-21-5p complexes were conjugated within an injectable hydrogel matrix via pH-responsive bonds to form Gel@MSN/miR-21-5p, which accurately released MSN/miR-21-5p complexes only in the acidic infarct area.

Here, we designed an injectable hydrogel loaded with MSN/miR-21-5p complexes (Gel@MSN/miR-21-5p) to deliver miR-21-5p in a two-stage mechanism: The first stage comprises pH-triggered on-demand delivery of MSN/miR-21-5p complexes from the hydrogel matrix in acidic infarct areas, and the second stage involves intracellular delivery of miR-21-5p from MSN/miR-21-5p complexes. This drug delivery system is designed to harness the synergy of inflammation suppression and angiogenesis enhancement in treating MI, the efficacy of which was evaluated in a clinically relevant MI swine model.

RESULTS
Preparation and characterization of an injectable hydrogel drug delivery system (Gel@MSN/miR-21-5p)
Amino (-NH$_2$) and trimethylamine [-N(CH$_3$)$_3$, TMA] functionalized MSNs (MSN-NH$_2$-TMA) were first synthesized (fig. S1A), which had positive charges for miRNA loading (fig. S1B). The miRNA-loading capacity of the MSN-NH$_2$-TMA complex was quantitatively evaluated by a gel retardation assay and ζ potential measurements (fig. S1C), which showed complete encapsulation of miRNA when the mass ratio between the MSN-NH$_2$-TMA complex and miRNA increased to 10:1. Subsequent studies were all using MSN/miRNA complexes with this ratio. Direct evidence of miRNAs loading in MSNs was also provided by transmission electron microscopy (fig. S1D) and energy-dispersive x-ray spectroscopy (EDS) analysis (fig. S1E), which revealed obvious miRNAs residing in MSN pores and signals corresponding to the element P from loaded miRNAs.

Gel@MSN/miR-21-5p was fabricated by mixing the MSN/miR-21-5p complex aqueous solution (30 wt%) with an aqueous solution of α-CD (66.7 mg/ml) and aldehyde-capped polyethylene glycol (PEG$_{CHO}$; 66.7 mg/ml). The hydrogel matrix had a porous structure with pore sizes of around 10 μm in diameter and MSN/miR-21-5p complexes covering the wall surface (fig. S1F). Scanning electron microscope image of the injectable colloidal hydrogel (Gel@MSN) showed plenty of MSNs conjugated in the hydrogel (red arrows). The presence of MSNs was also confirmed by EDS, which showed an obvious elemental signal of Si (fig. S1G). Hydrogel formation resulted from two interactions (fig. S2): (i) hydrophobic interaction between cyclodextrins (CDs) along the PEG$_{CHO}$ chains (27) and (ii) Schiff base between the NH$_2$ group from MSNs and the aldehyde (CHO) group from PEG$_{CHO}$/CD complexes. The stepwise gelation was confirmed

by comparing different gelation processes between the MSN/PEG$_{CHO}$/CD (group with both Schiff base and hydrophobic interaction) and control groups (PEG/MSN, group without hydrophobic interactions and Schiff bases; PEG/MSN/CD, group only with hydrophobic interactions) (fig. S3A) as well as the different rheological characterization of the resulting hydrogels (fig. S3, B and C). The cross-linking relies on hydrophobic and Schiff interactions, which are relatively weaker than conventional covalent bonds. The liquid-gel transition takes approximately 5 min, after which point the hydrogel is injected into the infarct area. The weak interaction allows the hydrogel to exhibit a shear-thinning property, which permitted it to switch from hydrogel to fluid during injection and subsequently formed a firm hydrogel at the MI area along with the further cross-linking process (fig. S3D). The retention property of the hydrogel in the beating heart was also evaluated. During bench testing, hydrogel (labeled with blue dye) was injected into myocardium tissue, and no detachment or cracks were observed between the hydrogel and tissue after bending, distorting, long-time immersing underwater, or stretching (fig. S3E).

The MSN/miRNA complexes were conjugated onto an injectable hydrogel by Schiff bonds. The Schiff base bond is stable at pH 7.4 but is disrupted in an acidic environment (pH 6.8) (fig. S3, F to H), enabling an on-demand release of MSN/miRNA (step 3 in fig. S2B) (28, 29). The ^{1}H NMR (nuclear magnetic resonance) of 1,6-diaminohexane (HDA) functionalized PEG with Schiff base in between (HDA-PEG-HDA) after incubation in phosphate-buffered saline (PBS) buffer with pH 7.4 (red line) and pH 6.8 (black line) for 24 hours, which presented a clear proton peak of aldehyde only in the pH 6.8 treated group, demonstrating the high stability of Schiff base bonds at pH 7.4 and its gradual cleavage to form an aldehyde group at an acidic environment (fig. S3F). The gel permeation chromatography results of HDA functionalized PEG with Schiff base in between (HDA-PEG-HDA) after incubation in PBS buffer with pH 7.4 (i) and pH 6.8 (ii) for 24 hours, which presented an obvious drop of molecule weight only in the pH 6.8 treated group. Moreover, the molecule weight loss is close to twice the molecule weight of HDA, indicating the separation of HDA with PEG, due to the break of Schiff base (fig. S3H). These data comprehensively demonstrated the high stability of Schiff base bonds at pH 7.4 and its gradual cleavage at the slightly acidic environment.

The on-demand release profile was characterized in PBS buffer with pH 7.4 and pH 6.8 [which respectively simulated the microenvironment of healthy tissue (pH 7.4) and infarcted myocardium (pH 6.8)] (30, 31). There was a sustained release of MSN/miRNA complexes from the hydrogel matrix with ~75% release after 7 days at pH 6.8 (fig. S3I). In contrast, only ~6% MSN/miRNA was released from the hydrogel after 7 days at pH 7.4, which could be attributed to the diffusion of MSN/miR-21-5p at the different hydrogel degradation rates under different pH conditions (fig. S3I). The miRNA release from the MSN/miRNA complexes is presented in fig. S3J, which shows that a further decrease in the pH value to 5 (simulated intracellular endosomes and lysosomes environment) (32) could trigger miRNA release from MSN/miRNA complexes, leading to a cumulative release of miRNA of up to 60% over 48 hours.

Hydrogel degradation in vitro was monitored by measuring dry weight loss as a function of time following incubation in PBS (pH 6.8) at 37°C (fig. S3K). As shown in fig. S3K, Gel@MSN/miRNA lost approximately 93% of the initial gel mass within 20 days. For in vivo measurements, the PEG frame of the hydrogel was labeled by fluorescent dye. Following injection, the fluorescence signal in the injected

area was detected at the indicated time points. Figure S4 shows that the fluorescence signal decay is down to 67% at day 3 and 16% at day 14. At day 28, we could not detect any fluorescence signal, indicating that the hydrogel was completely degraded.

The retention of MSNs in vivo was monitored by fluorescence in vivo imaging system (IVIS) imaging at the indicated time points. Figure S5 shows that the fluorescence signal decay is down to 54% at day 3, 18% at day 14, and 2% at day 28, indicating that accumulation of MSNs was gradually decreased at tissue. At day 36, no positive signal was observed, indicating that almost no residual MSNs could be detectable at tissue.

In vitro bioactivity of MSNs/miR-21-5p
To assess the in vitro uptake of the MSN/miR-21-5p complex by endothelial cells, the miR-21-5p was labeled with Cy3 (orange-red), the MSNs were labeled with fluorescein isothiocyanate (FITC) (green), and the cell nuclei were stained with 4′,6-diamidino-2-phenylindole (DAPI) (blue). For in vitro uptake analysis, endothelial cells were cocultured with MSN/miR-NC complexes or MSN/miR-21-5p complexes. The confocal images and quantification analysis showed that MSN/miR-21-5p complexes showed high transfection efficiency of miR-21-5p and resulted in an approximately 37-fold enhanced miR-21-5p levels in endothelial cells compared to that of control cells (Fig. 1, A and B). Representative profiles from the flow cytometry analysis revealed that the CD31 expression level was 96.5% in endothelial cells (Fig. 1C). Flow cytometry analysis indicated that more than 70% of endothelial cells internalized the MSN/miR-21-5p complexes (identified by the CD31$^+$Cy3$^+$) (Fig. 1D). The cytokine levels were determined by Western blot and real-time quantitative polymerase chain reaction (PCR) assay. Figure 1E shows that compared to the endothelial cell group and the MSN/miR-NC–treated group, MSN/miR-21-5p significantly promoted the expression of proangiogenic cytokines (VEGFA and PDGF-BB) from endothelial cells. MSN/miR-21-5p–treated endothelial cells also had increased capillary tube network formation (as measured by branch points and total tube length via tube formation assay) (as shown in Fig. 1G). We then simulated serum-free and hypoxic infarct-like conditions in vitro to assess the protective effect of MSN/miR-21-5p on the hypoxia/ischemia-induced cardiomyocyte apoptosis (Fig. 1H). The cardiomyocytes were exposed to a combination of ischemic/hypoxic conditions for 24 hours. Endothelial cells were pretreated with MSN/miR-21-5p or MSN/miR-NC and then cocultured with cardiomyocytes subjected to hypoxia/ischemia. Notably, at 24 hours of coculture, we found that coculture with MSN/miR-21-5p–treated endothelial cells reduced the apoptosis of hypoxia/ischemia-induced cardiomyocytes. This correlated with increased secretion of proangiogenic cytokines (VEGFA and PDGF-BB) from endothelial cells treated with MSN/miR-21-5p (Fig. 1, I and J). Previous studies demonstrated that VEGFA or PDGF-BB inhibits apoptosis (33, 34). These data may suggest that miR-21-5p–induced expression of proangiogenic factors in endothelial cells could prevent cardiomyocytes from undergoing apoptosis under ischemic and hypoxic conditions.

To understand the in vitro immunomodulatory effect of MSN/miR-21-5p complexes, MSN/miR-NC complexes or MSN/miR-21-5p complexes were cocultured with isolated macrophages. MSNs were labeled with FITC (green), and miR-21-5p was labeled with Cy3 (red). Representative profiles from the flow cytometry analysis revealed that the F4/80 expression level was 98.2% in isolated macrophages (Fig. 1C). The confocal images and quantification analyses showed

that MSN/miR-21-5p complexes had high uptake efficiency in macrophages. Flow cytometry analysis indicated that more than 80% of macrophages took up the MSN/miR-21-5p complexes (identified by the F4/80$^+$Cy3$^+$ staining pattern) (Fig. 1D). We then examined whether the uptake of the MSN/miR-21-5p complexes by macrophages could reduce the inflammatory response. For this purpose, a proinflammatory response was induced by injection of lipopolysaccharide (LPS), a potent inducer of inflammatory response (35), into the peritoneum of mice, and macrophages from the treated mice were collected. Figure 1F shows that the inflammation of the LPS-treated macrophages (LPS-macrophages) was markedly suppressed following uptake of the MSN/miR-21-5p complexes, as indicated by the notable decrease in the expression of tumor necrosis factor-α (TNF-α), interleukin-1β (IL-1β), and IL-6, which are typical cytokines involved in the inflammatory response. These data suggest that the MSN/miR-21-5p complexes released from Gel@MSN/miR-21-5p simultaneously reduced proinflammatory cytokines and increased proangiogenic factors in vitro. The enhanced proangiogenic factors from endothelial cells could effectively prevent cardiomyocytes from apoptosis under ischemic and hypoxic conditions.

The mechanism underlying MSN/miR-21-5p complex modulation of the immune response
To obtain insight into the mechanism by which the MSN/miR-21-5p complex acts on macrophages to modulate the immune response, we performed a proteome analysis of protein alterations in macrophages. We collected three replicates of LPS-induced macrophages (inflammatory stage macrophages) treated with MSN/miR-NC, MSN/miR-21-5p, or pure MSNs. Untreated LPS-macrophages were used as a negative control. We used a label-free quantitative proteomic approach. Hierarchical clustering analysis of the data revealed that the protein expression patterns of the three treatment groups (MSN/miR-NC, MSN/miR-21-5p, or pure MSNs) were obviously different from that of LPS-macrophages without treatment, while the protein expression patterns of the three groups were similar (Fig. 2A). This consistently indicated that the function of immunomodulation originates from the MSNs themselves.

Current reports showed that the reduced inflammatory response elicited by MSN resulted from the reduction of transcription factor nuclear κ B (NFκB), caspase-3, and IL-12 (36). The NFκB signaling plays a major role in innate immunity and inflammatory responses. It was shown that the NFκB signaling pathway plays important roles in MSN-regulated inflammation (37), but the exact mechanism leading to this effect was still obscure.

The present study used the GSEA (gene set enrichment analysis) method to examine the distribution of the functionally related KEGG (Kyoto Encyclopedia of Genes and Genomes) pathway gene sets within the ranked gene list. GSEA showed that there were groups of genes negatively correlated with the immune response after MSN treatments. The majority of genes that were differentially expressed in macrophages after MSN treatments were enriched in several pathways, such as neutrophil degranulation, Toll-like receptor (TLR) signaling pathway, and MyD88 deficiency (Fig. 2B). TLR activation and MyD88 (a downstream adapter of TLR pathways) play important roles in the NFκB signaling pathway (37), stimulation of which may lead to activation of NFκB signaling and eventually lead to proinflammatory responses and progression to fibrous tissues (38, 39).

We found that abundance of proteins (TLR1, TLR2, TLR4, TLR3, TLR7, TLR8, TLR9, CD14, RAC1, and TAB1) involved in TLR
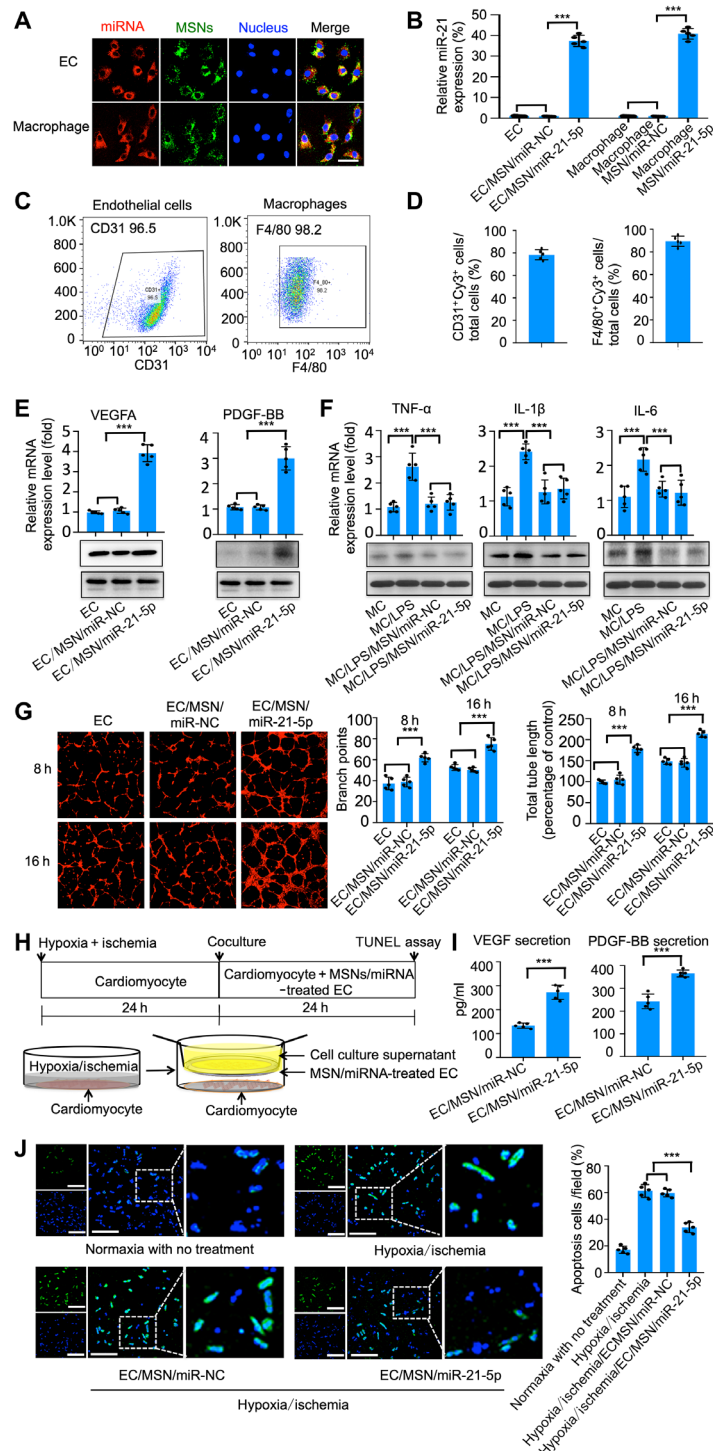
Fig. 1. In vitro bioactivity of the MSN/miR-21-5p complex. (**A**) In vitro uptake of the MSN/miR-21-5p complex by adherent endothelial cells (ECs) and macrophages (MCs). (**B**) In vitro transfection efficiency of miR-21-5p was determined by quantifying the miRNA level using real-time quantitative PCR. (**C**) Representative flow cytometry analysis of CD31 levels in ECs and F4/80 levels in MCs. (**D**) In vitro uptake of the MSN/miR-21-5p complex by ECs and MCs was determined by quantifying the double-positive cells (CD31 or F4/80 and Cy3) using flow cytometric analysis. The protein expression levels of VEGFA and PDGF-BB in endothelial cells (**E**) and tumor necrosis factor-α (TNF-α), interleukin-1β (IL-1β), and IL-6 in macrophages (**F**) were determined by the real-time quantitative PCR and Western blot analysis. (**G**) The endothelial cells that formed three-dimensional (3D) capillary-like tubular structures were evaluated at indicated times (8 and 16 hours). (**H**) Schematic diagram of the experimental setup. TUNEL, terminal deoxynucleotidyl transferase–mediated deoxyuridine triphosphate nick end labeling. (**I**) Apoptosis-positive cardiomyocytes from these treatment groups were further quantified. (**J**) Protein levels of secreted proangiogenic factors were determined by enzyme-linked immunosorbent assay (ELISA) analysis of cell supernatants from the MSN/miRNA-treated ECs (scale bars, 50 μm). *$P < 0.05$ and ***$P < 0.01$. All experiments were carried out in triplicate. $n = 5$ per group. The data are shown as means ± SD. Photo credit: Yan Li, Shanghai Ninth People's Hospital, College of Stomatology, Shanghai Jiao Tong University School of Medicine, Shanghai 200011, China.
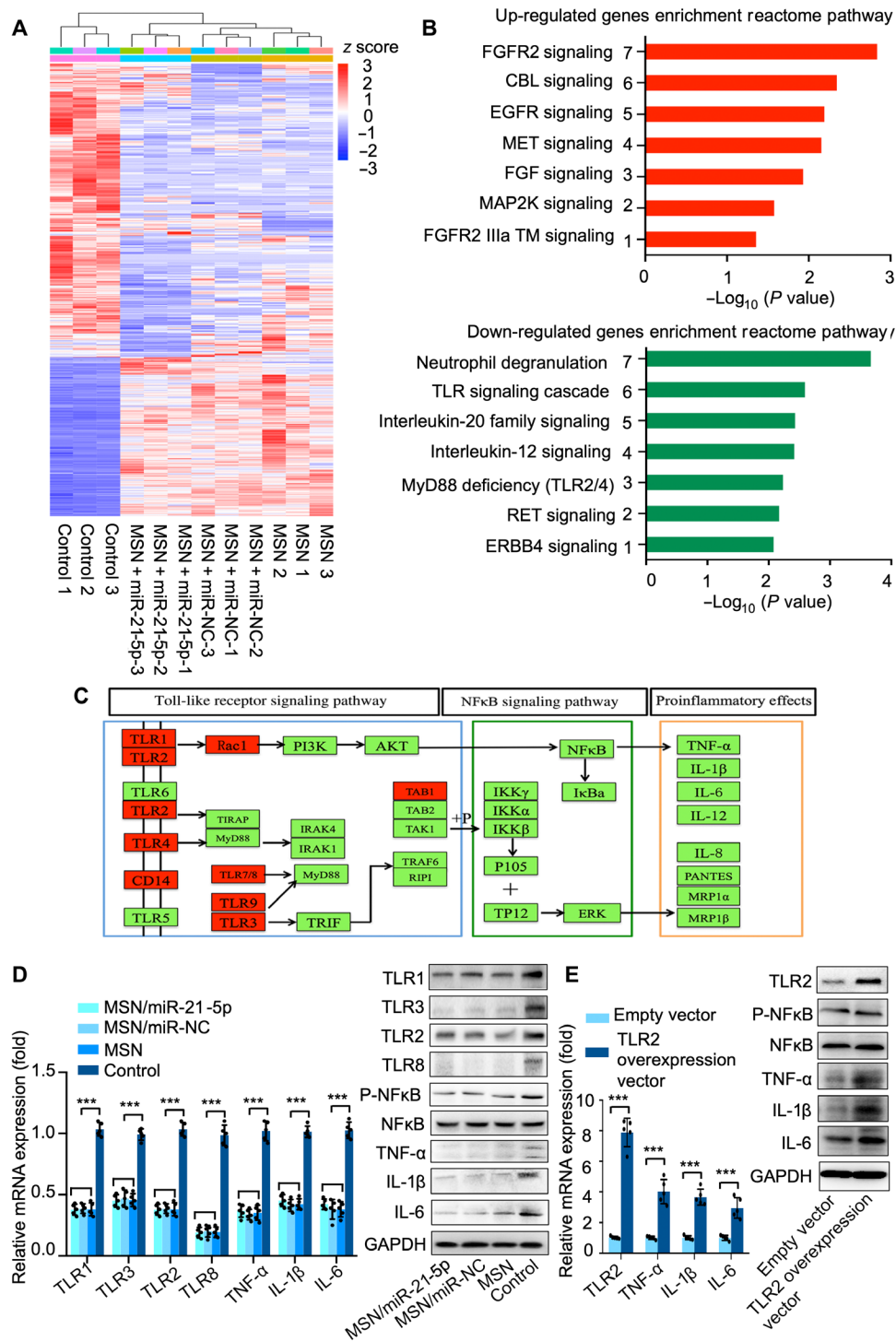
Fig. 2. The mechanism underlying the effects of the MSN complex on modifying the immune response. (**A**) A heatmap of selected proteins representing major altered signaling pathways in three datasets of macrophages treated with MSNs, MSN/miR-NC, or MSN/miR-21-5p complexes. Macrophages with no treatment were used as a negative control. The color bar indicates normalized z score intensity–based absolute quantification. (**B**) KEGG (Kyoto Encyclopedia of Genes and Genomes) pathway analysis of both up- and down-regulated pathways in macrophages after MSN treatment. The most significant pathways in the phosphoproteome are plotted on the x axis as the $-\log_{10}$ of the P value, compared with the proteome. (**C**) KEGG pathway map of Toll-like signaling pathway. Proteins shown with red backgrounds are down-regulated in macrophages after MSN complex treatments when compared with macrophages with no treatment, as determined by pathway analysis. (**D**) Real-time quantitative PCR and Western blot analysis of TLR1, TLR2, TLR3, TLR8, P-NFκB, TNF-α, IL-1β, and IL-6 protein content alteration in macrophages after treatment with MSNs, MSN/miR-NC, or MSN/miR-21-5p complexes. (**E**) Real-time quantitative PCR and Western blot analysis of P-NFκB, TNF-α, IL-1β, and IL-6 protein content alteration in MSN/miR-21-5p complex–treated macrophages that overexpress TLR2 with the TLR2 overexpression vector. ***$P < 0.01$. $n = 3$ per group. The data are shown as means ± SD. Photo credit: Yan Li, Shanghai Ninth People's Hospital, College of Stomatology, Shanghai Jiao Tong University School of Medicine, Shanghai 200011, China.

signaling was down-regulated in macrophages after MSN treatments, indicating that TLR signal transduction pathway activity decreased in response to MSN treatment (Fig. 2C). The most significantly down-regulated genes are TLR1, TLR2, TLR3, and TLR8, which had more than threefold change.

To gain further insight into the mechanism by which MSNs modulated the immune response through the TLR signaling pathway, we examined protein alterations of TLR1, TLR2, TLR3, and TLR8 within macrophages after MSN treatment (Fig. 2D). We found that the mRNA and protein expressions of TLR1, TLR2, TLR3, and TLR8 cytokines were substantially lower in all MSN-treated groups. Meanwhile, NFκB signaling pathway and downstream proinflammatory cytokines (TNF-α, IL-1β, and IL-6) were inhibited, which is consistent with previous findings that TLRs act as primary sensors that elicit innate immune responses and activate NFκB signaling (Fig. 2D). Among the known TLRs, TLR2 has been characterized extensively as an inducer of proinflammatory cytokines. To determine whether MSNs modulated the immune response by down-regulating TLR2, we first treated macrophages with MSNs and then transfected MSN-treated macrophages with a TLR2 overexpression plasmid vector or empty vectors. We found that the NFκB signaling pathway was up-regulated in macrophages transfected with the TLR2 overexpression vector compared to the empty vector control group. Consistently, the amounts of TNF-α, IL-1β, and IL-6 protein in macrophages were increased by transfection with the TLR2 overexpression vector (Fig. 2E). These comprehensive data suggest that MSNs modulated immune response through down-regulating TLR2, which inhibited the activation of NFκB signaling and subsequently decreased the release of proinflammatory cytokines (TNF-α, IL-1β, and IL-6) (fig. S6).

The mechanism underlying the MSN/miR-21-5p complex promoting angiogenesis

To obtain insight into the mechanism underlying miR-21-5p–enhanced angiogenesis, we performed a proteogenomic analysis of protein alterations in endothelial cells after miR-21-5p treatment. We collected three replicates of endothelial cells after treatment with MSN/miR-NC or MSN/miR-21-5p. We applied a label-free quantitative proteomic approach. Hierarchical clustering analysis of the data revealed that the genes could be assigned into two groups based on their protein expression patterns, and the assigned groups matched with the groups by treatment (Fig. 3A). GSEA revealed that there were groups of genes positively correlated with angiogenesis after MSN/miR-21-5p treatment. KEGG analysis suggested that the MSN/miR-21-5p treatment groups were positively associated with key angiogenic signaling pathways (Fig. 3B). Compared to MSN/miR-NC–treated endothelial cells, MSN/miR-21-5p–treated endothelial cells had a larger number of proteins enriched in pathways such as vascular endothelial growth factor (VEGF) signaling pathway and platelet-derived growth factor (PDGF) signaling pathway (Fig. 3B). VEGF is the major mediator in endothelial cells and is considered to be a crucial signal transducer in angiogenesis. The binding of VEGF to the VEGF receptor leads to a cascade of signaling pathways, including ERK-MAPK (extracellular signal–regulated kinase/mitogen-activated protein kinase) signaling, which particularly plays a central role in angiogenesis. Therefore, we focused on ERK-MAPK signaling in MSN/miR-21-5p–treated endothelial cells and found that the levels of phospho-Erk1/2, phospho-FAK, phospho-P38, phospho-AKT, VEGFA, and PDGF-BB were up-regulated in the MSN/miR-NC group,

indicating that miR-21-5p could enhance VEGFA expression and subsequently lead to ERK-MAPK signaling activation (Fig. 3C).

To gain further insight into the mechanism by which miR-21-5p promotes angiogenesis, we used a miRNA database to predict the potential target genes of miR-21-5p and found that SPRY1 has a miR-21-5p binding site in its 3′ untranslated region (UTR). The amount of SPRY1 protein in endothelial cells was down-regulated by MSN/miR-21-5p treatment but not by MSN/miR-NC treatment, whereas we found no difference in SPRY1 mRNA levels between the two groups (Fig. 3D). To determine whether miR-21-5p functionally targets SPRY1 to promote angiogenesis, we overexpressed SPRY1 in endothelial cells. We found that phospho-Erk1/2, phospho-FAK, phospho-P38, phospho-AKT, VEGFA, and PDGF-BB levels were down-regulated in MSN/miR-21-5p–treated endothelial cells transfected with SPRY1 overexpression plasmid vector, compared to cells transfected with the empty vector (Fig. 3E). To test whether miR-21-5p directly targets SPRY1, we constructed luciferase reporters that had either the wild-type (WT) SPRY1 3′UTR or an SPRY1 3′UTR containing mutations at the miR-21-5p binding site (Fig. 3F). First, we found that MSN/miR-21-5p, but not MSN/miR-NC, substantially inhibited the luciferase reporter activity of the WT SPRY1 3′UTR. Second, the luciferase reporter activity of the SPRY1mRNA with the mutated 3′UTR was not suppressed by MSN/miR-21-5p (Fig. 3G). These comprehensive data suggest that delivery of miR-21-5p using MSN/miR-21-5p complexes promotes angiogenesis by targeting SPRY1 and subsequently activating the VEGF-induced ERK-MAPK signaling pathway (fig. S6). Detailed predicted miR-21-5p targets by Venn diagram analysis were revealed in fig. S7.

Therapeutic efficacy of Gel@MSN/miR-21-5p in the morphology and pumping effectiveness of the heart after MI in vivo

The in vivo efficacy of Gel@MSN/miR-21-5p was evaluated in an induced MI swine model. Coronary arteries were identified and ligated to induce a uniform and consistent MI, and the morphology and pumping effectiveness of the heart were evaluated ~45 min after the MI induction. The MI animals were then randomly divided into four groups receiving saline (negative control), agomiR-21-5p (a commercially available agent used to up-regulate endogenous miR-21-5p level), Gel@MSN/miR-NC, and Gel@MSN/miR-21-5p injection. Sham-operated animals served as a positive control. Morphological and functional assessments were performed using the modified Simpson method, which can accurately calculate left ventricular ejection fraction (LV EF) to detect any early echocardiographic changes. Changes in the morphology and pumping effectiveness of the heart were assessed through measurements of LV end diastolic volume (LVEDV), LV end systolic volume (LVESV), EF, and LV end diastolic dimension (LVEDd). Representative echocardiography images of short-axis views for each treatment group at baseline (before MI) and 45 min, 14 days, and 28 days after MI are shown in Fig. 4A. MI caused a substantial reduction in LV function 45 min after induction, as indicated by an absolute 20% decline in the EF. The morphological and functional parameters were slightly improved in the agomiR-21-5p and Gel@MSN/miR-NC groups compared with the saline negative control group at 14 and 28 days after MI, indicating that either miR-21-5p or MSNs alone could improve the morphology and pumping effectiveness of the heart but only to a limited degree (~an absolute 4 to 5% increase in EF values at 28 days, as compared to the saline group). More substantial improvement was achieved in
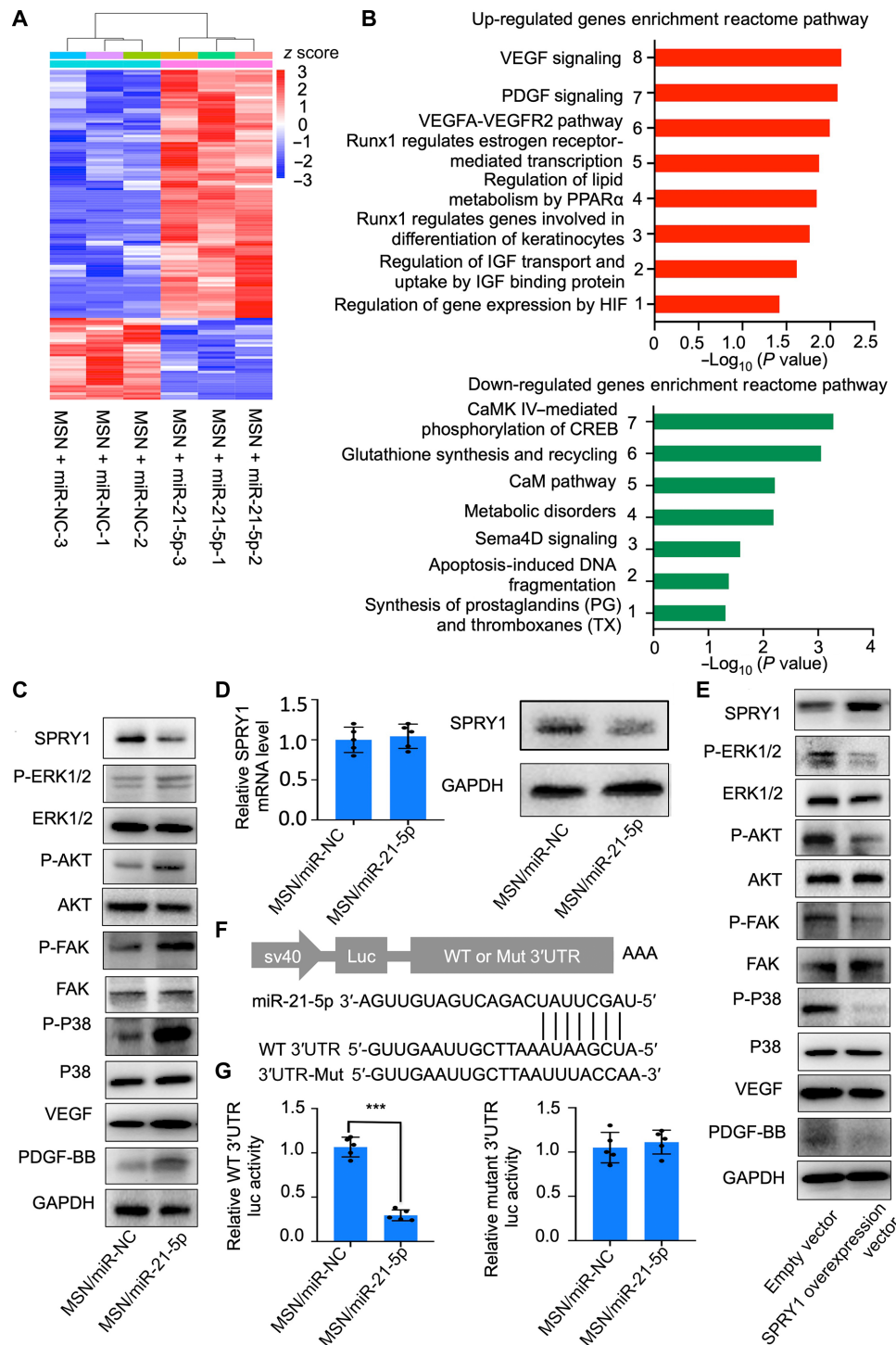
Fig. 3. The mechanism underlying how the MSN/miR-21-5p complex promotes angiogenesis. (**A**) A heatmap of selected proteins representing strongly altered signaling pathways in three datasets of endothelial cells treated with MSN/miR-NC or MSN/miR-21-5p complexes. (**B**) KEGG pathway analysis of both up- and down-regulated pathways in endothelial cells after MSN/miR-21-5p complex treatment. (**C**) Western blot analysis of changes in SPRY1, P-ERK1/2, P-FAK, P-p38, P-AKT, VEGFA, and PDGF-BB protein content alteration in endothelial cells after treatment with the MSN/miR-21-5p complex. (**D**) The effect of MSN/miR-21-5p or MSN/miR-NC on SPRY1 mRNA levels (left) and SPRY1 protein levels (right) in endothelial cells. (**E**) Schematic diagram illustrating the design of luciferase reporters with the WT SPRY1 3′ untranslated region (WT 3′UTR) or the site-directed mutant SPRY1 3′UTR (3′UTR-Mut). (**F**) The effect of MSN/miR-21-5p on luciferase activity in endothelial cells transfected with either the WT SPRY1 3′UTR reporter (left) or the mutant *SPRY1* 3′UTR reporter (right). (**G**) Western blot analysis of P-ERK1/2, P-FAK, P-p38, P-AKT, VEGFA, and PDGF-BB protein level alteration in MSN/miR-21-5p complex–treated endothelial cells after overexpressing SPRY1 with the SPRY1 overexpression vector. *$P < 0.05$ and ***$P < 0.01$. $n = 3$ per group. The data are shown as means ± SD. Photo credit: Yan Li, Shanghai Ninth People's Hospital, College of Stomatology, Shanghai Jiao Tong University School of Medicine, Shanghai 200011, China.
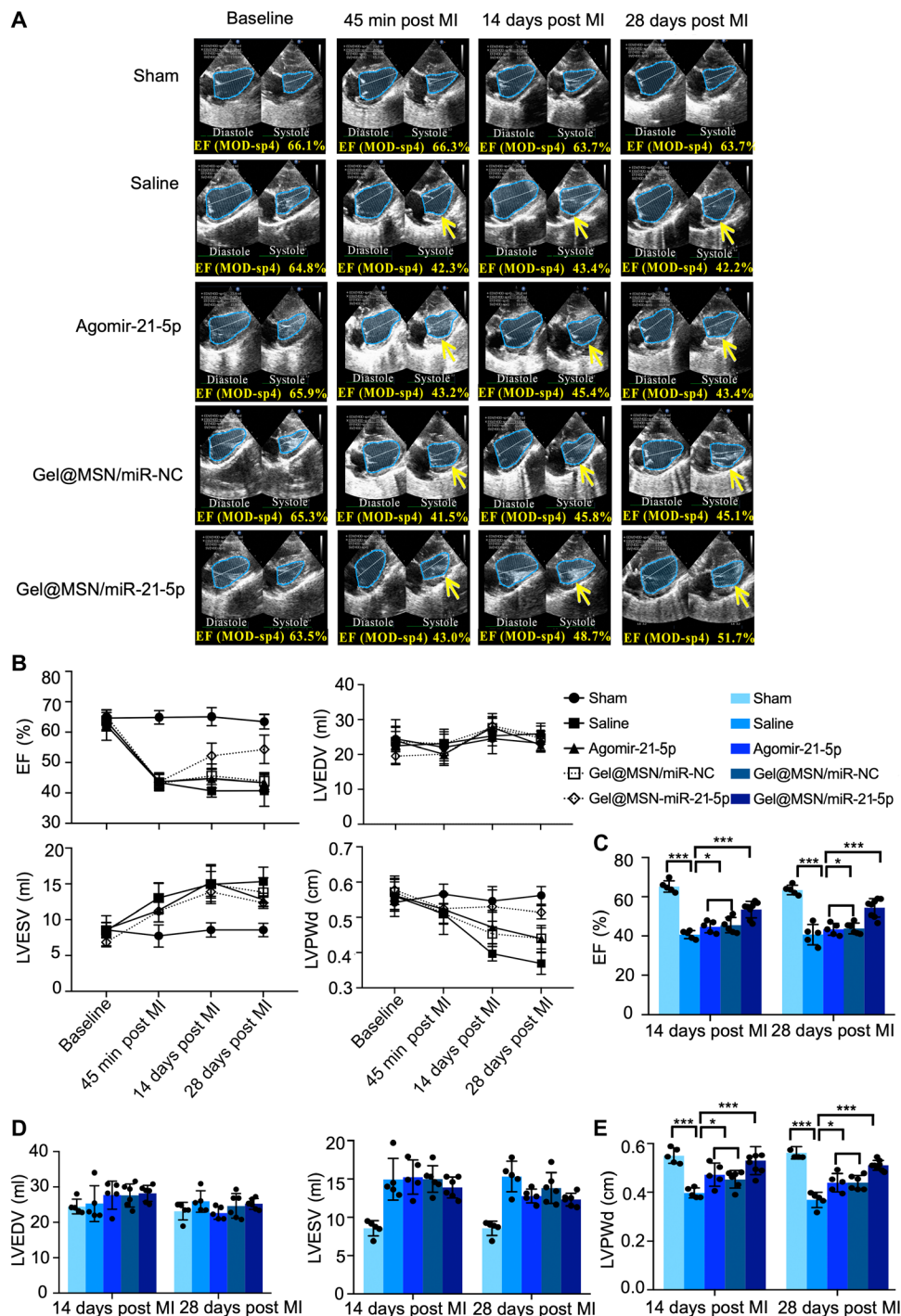
Fig. 4. Gel@MSN/miR-21-5p attenuates adverse LV remodeling and improves pumping effectiveness of the heart after MI. (**A**) Representative echocardiography imaging by the modified Simpson method of short-axis views for each treatment group at baseline and 45 min, 14 days, and 28 days after MI. The site of the infarct zone is shown by arrows. Notable chamber dilation and wall thinning occurred at 28 days following MI, consistent with the adverse remodeling process. (**B**) Time course analysis of the EF, LVEDV, LVESV, and LVPWd. (**C**) MI caused a gradual decline in the EF over 28 days, which was notably attenuated by Gel@MSN/miR-21-5p. (**D**) MI caused a gradual increase in the LVEDV at day 14 and day 28. The LVEDV of the Gel@MSN/miR-21-5p treatment group was substantially attenuated compared with those of the other three treatment groups. (**E**) MI caused progressive thinning of the LVPWd thickness at the diastole, which was attenuated by Gel@MSN/miR-NC and agomiR-21-5p treatment and further attenuated by Gel@MSN/miR-21-5p treatment at day 14 and day 28. *$P < 0.05$ and ***$P < 0.01$. Sham, $n = 3$; MI/saline, $n = 5$; MI/agomir, $n = 5$; MI/ Gel@MSN/miR-NC, $n = 6$; and MI/Gel@MSN/miR-21-5p, $n = 6$. The data are shown as the means ± SD. Photo credit: Yan Li, Shanghai Ninth People's Hospital, College of Stomatology, Shanghai Jiao Tong University School of Medicine, Shanghai 200011, China.

the Gel@MSN/miR-21-5p group, with an approximately absolute 10% increase in the LV EF values at 28 days after MI. Time course echo-cardiography assessment over the 28-day study period is shown in Fig. 4B. These data suggest the importance of the therapeutic itself (miR-21-5p) as well as the delivery system (a two-stage delivery) in mitigating the negative LV remodeling and improving the morphology and pumping effectiveness of the heart after MI.

Representative delayed-enhancement computed tomography (CT) images of cross-sectional planes of hearts from two-axis (long axis and short axis) slices at day 28 after MI are shown in Fig. 5. The infarct
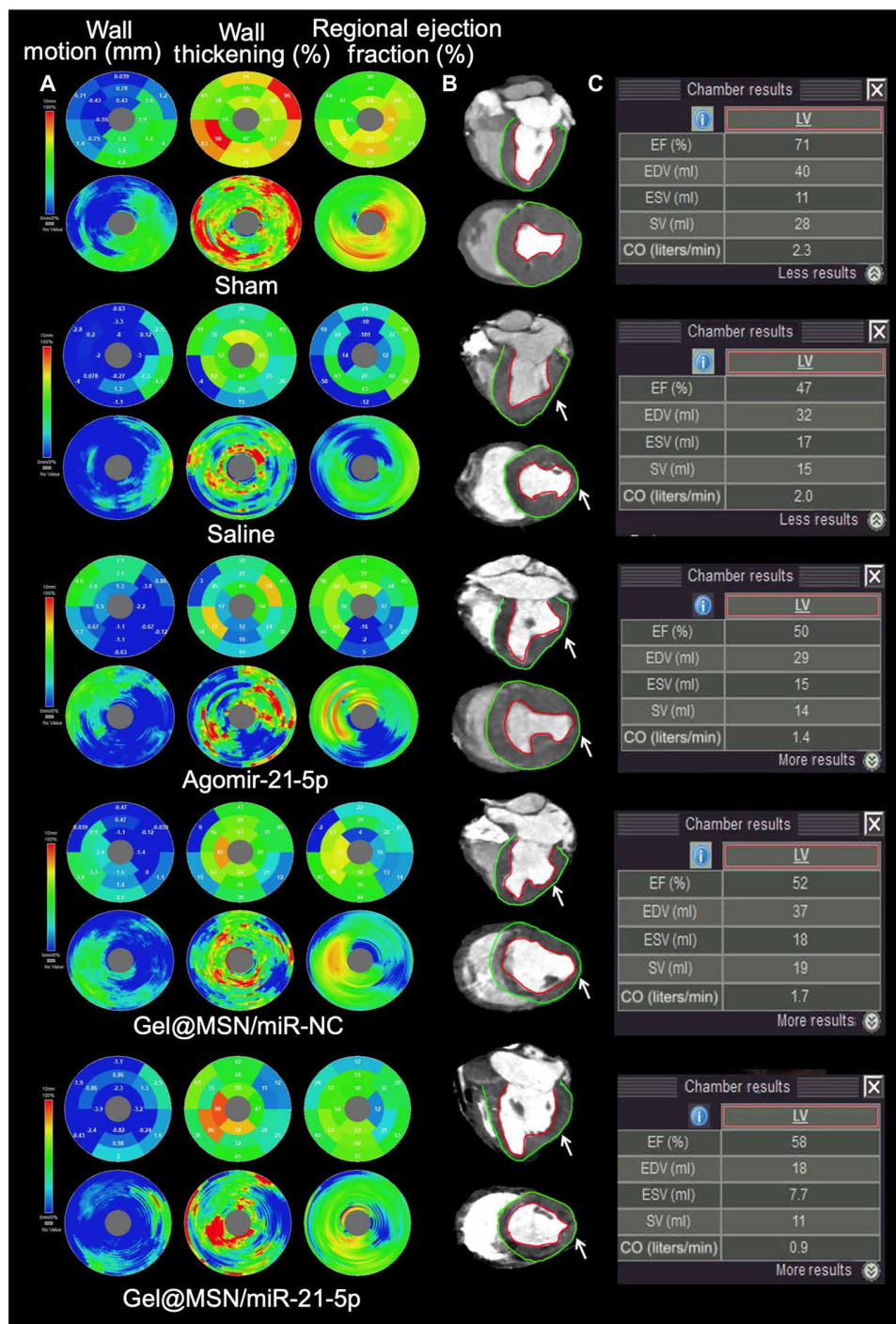
Fig. 5. Delayed enhancement CT analysis of LV segmentation. Representative delayed enhancement CT images of cross-sectional planes of hearts from two-axis (long axis and short axis) slices at day 28 after MI are shown. (**A**) Bull's eye plots display the LV wall thickness, wall motion, and regional EFs. (**B**) The infarct zone was characterized by wall thinning (identified by white arrows). (**C**) Global cardiac functional measures such as cardiac output, stroke volume, and EF are shown in the inserted table. Photo credit: Yan Li, Shanghai Ninth People's Hospital, College of Stomatology, Shanghai Jiao Tong University School of Medicine, Shanghai 200011, China.

regions in the LV posterior wall were characterized by wall thinning (identified by red counterstain). Analysis of systolic LV wall thickness showed that the wall thickness in the infarcted zone was retained in the agomiR-21-5p– and Gel@MSN/miR-NC–treated groups 28 days after MI to a limited degree (marked with white arrows) compared to that in the saline-treated group. LV wall thickness in the infarcted zone was further persevered with the Gel@MSN/miR-21-5p–treated group. Bull's eye plots (Fig. 5A) display LV wall thickness, wall motion, and regional EFs. Global cardiac functional measures such as LVEDV, LVEDV, and EF are shown in the inserted table.

Infarct size as measured by tetraphenyl tetrazolium chloride (TTC) staining also showed that the Gel@MSN/miR-21-5p group had the smallest infarct size (Fig. 6A; paired multiple slices of an infarcted heart in the same pigs shown in fig. S8). The histological characterization of the LV sections from the infarct region at 28 days after MI showed that the infarcted regions in pigs injected with Gel@MSN/miR-21-5p present preserved distinct and thick muscle layers. However, moderately thickened muscle was observed in the agomiR-21-5p and Gel@MSN/miR-NC groups, and obvious fibrillary layers were observed in the saline group. The muscle layers were verified to be cardiomyocytes by anti–cardiac troponin-T staining (Fig. 6B). Masson's trichrome staining showed approximately two times less fibrous content in the Gel@MSN/miR-21-5p group than in the saline group (Fig. 6D). These observations provided evidence that Gel@MSN/miR-21-5p treatment could effectively attenuate fibrosis and improve cardiac remodeling after MI.

The in vivo data relating to drug release duration and efficacy of MSNs and miRNA delivery by Gel@MSN/miR-21-5p were characterized. Confocal images and quantification analysis showed that more than 60% of macrophages (identified by the F4/80^{+} marker) or endothelial cells (identified by the CD31^{+} marker) took up the MSN/miR-21-5p complexes 1 day after injection (Fig. 7). Furthermore, the high intracellular transfection efficacy was sustained up to ~28 days, as evidenced by an approximately twofold increase in endogenous miR-21-5p levels (Fig. 7), which could contribute to the improved morphology and pumping effectiveness of the heart.

We further compared the effects of MSN/miR-21-5p complexes without a hydrogel matrix (MSN/miR-21-5p alone) and with a hydrogel matrix (Gel@MSN/miR-21-5p) on treating MI. The morphological and functional parameters of the MSN/miR-21-5p group alone were worse than those of the Gel@MSN/miR-21-5p group at 14 and 28 days, and the parameters did not improve over time. The Gel@MSN/miR-21-5p delivery system provided sustained release of miR-21-5p (fig. S9) and sustained a superior therapeutic benefit compared to that from a bolus shot of MSN/miR-21-5p (fig. S10). Histological examination and the quantification of the total infarct size showed similar results. These data suggest that the hydrogel matrix could maintain a long-term drug release, which is important to achieve a persistent therapeutic effect. The hearts were harvested at 28 days after MI for fluorescent imaging, RNA extraction, and real-time quantitative PCR analysis. The fluorescent images showed that the areas of FITC and Cy3 fluorescence enhancement exactly overlapped with the infarct region (Fig. 8A). The confocal images and quantification of miR-21-5p levels showed that MSN/miRNA complexes were effectively transfected into cells within the infarct region in vivo (Fig. 8B). These data indicate that the hydrogel matrix achieved localized sustained drug release, triggered by the acidic microenvironment in the infarct region.

Proangiogenetic effect of Gel@MSN/miR-21-5p in the infarct region in vivo

The three-dimensional (3D) organization of the vascular network within the infarct regions was characterized by micro-CT angiography.
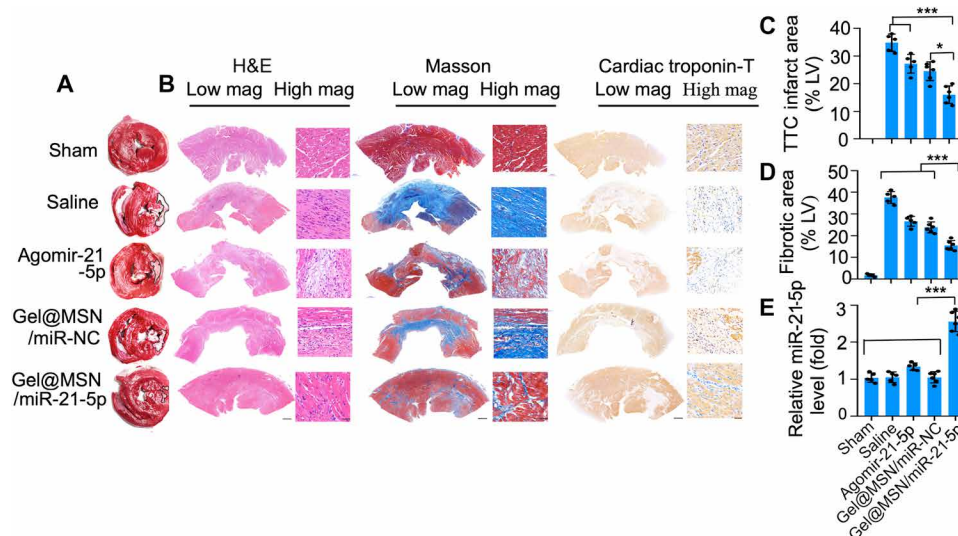

Fig. 6. Gel@MSN/miR-21-5p improved cardiac remodeling and reduced the infarct size after MI. A porcine model of MI was used to investigate the post-MI responsiveness of different groups to treatments. Healing at the infarct zone was analyzed after 28 days after treatment. (**A**) Representative image of TTC-stained hearts and morphometric measures of the infarct area from each group. White coloring in the TTC-stained sections indicates infarct zone and tissue necrosis. (**B**) Representative histological analysis of the infarcted myocardium among the treatment groups. H&E (left) staining, Masson's trichrome staining (middle), and immunohistochemistry staining for cardiac troponin T (right) 28 days after MI showed a loss of cardiomyocytes and collagen deposition, and interstitial fibrosis was substantially reduced in the infarct zone after the Gel@MSN/miR-21-5p treatment (scale bars, 2000 μm in the low-magnification images and 60 μm in the high-magnification images). Quantitative analysis showing the percentage of the TTC-negative infarct area (**C**) and fibrotic area (**D**). (**E**) miRNA transfection efficiency was investigated using real-time quantitative PCR at 28 days following MI. *$P < 0.05$ and ***$P < 0.01$. Sham, $n = 3$; MI/Saline, $n = 5$; MI/Agomir, $n = 5$; MI/Gel@MSN/miR-NC, $n = 6$; and MI/Gel@MSN/miR-21-5p, $n = 6$. The data are shown as the mean ± SD. Photo credit: Yan Li, Shanghai Ninth People's Hospital, College of Stomatology, Shanghai Jiao Tong University School of Medicine; Shanghai, 200011, China.
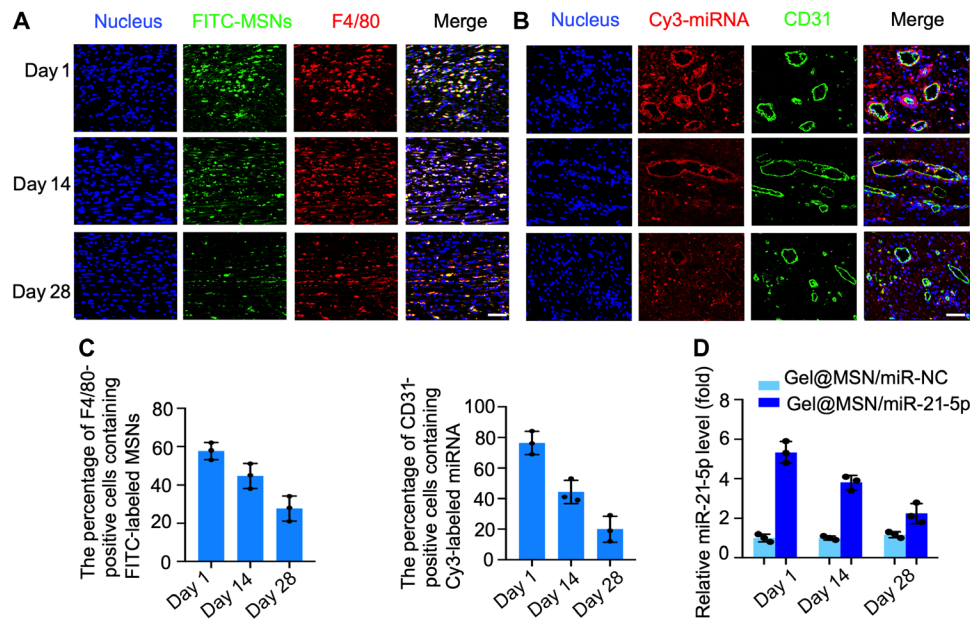
Fig. 7. Time course analysis of the transfection efficiency of Gel@MSN/miR-21-5p *in vivo*. MSNs were prelabeled with FITC (green), and miR-21-5p was prelabeled with Cy3 (red). The hydrogel (FITC-labeled Gel@MSN/miR-21-5p or Cy3-labeled Gel@MSN/miR-21-5p) was injected into the mid-myocardium of each target site in the pigs. The duration and efficiency of MSNs and miRNA delivery upon Gel@MSN/miR-21-5p injection were monitored using time course analysis at 1, 14, and 28 days after injection. (**A**) Histological sections of the infarct region in the Gel@MSN/miR-21-5p group were immunolabeled with the hematoxylin and eosin (H&E) macrophage marker F4/80. (**B**) Histological sections of the infarct region in the Gel@MSN/miR-21-5p group were immunolabeled with the endothelial marker CD31. Cell nuclei were counterstained with DAPI (blue). (**C**) F4/80$^+$FITC$^+$ and CD31$^+$Cy3$^+$ double-positive cells were quantified from at least eight high-resolution images acquired from at least eight different regions of each heart. (**D**) miR-21-5p levels were detected using real-time quantitative PCR at different time points. The transfection efficiency was determined by quantifying the miRNA level. Scale bars, 100 μm. *n* = 3 per group. The data are shown as means ± SD. Photo credit: Yan Li, Shanghai Ninth People's Hospital, College of Stomatology, Shanghai Jiao Tong University School of Medicine, Shanghai 200011, China.

The vascular density and volume were significantly improved with Gel@MSN/miR-21-5p (Fig. 9A). CD31 and α–smooth muscle actin (α-SMA) are typical biomarkers of endothelial cells and mural cells in blood vessels. Immunofluorescence characterization showed that expression levels of CD31 and α-SMA were significantly enhanced and that more newly formed vessels were observed in the Gel@MSN/miR-21-5p treatment group than in the other groups. These observations provided evidence that Gel@MSN/miR-21-5p treatment enhanced vascularization after MI.

Immunomodulatory effect of Gel@MSN/miR-21-5p in the infarct region in vivo

Immunofluorescence analysis of LV sections taken from the infarct region 1 day after MI showed that Gel@MSN/miR-21-5p effectively protected cardiomyocytes (fig. S11) and inhibited the expression of several key inflammatory mediators (TNF-α, IL-1β, and IL-6) (Fig. 10). Furthermore, concordant with reduced fibrotic area in the infarcted region in the Gel@MSN/miR-21-5p–treated group at 28 days after MI, the expression of key inflammatory mediators (TNF-α, IL-1β, and IL-6) was obviously reduced (fig. S12). These results suggested that Gel@MSN/miR-21-5p treatment modulated the immune response after MI by inhibiting the expression of proinflammatory cytokines.

The use of large-animal models of MI provides valuable information regarding the safety and efficacy of new therapies. Pig models offer an alternative because of their anatomical and physiological similarities to humans (*40*, *41*). The treatment groups used materials such as PEG derivatives, CD, silica, and miRNA, and an obvious

inflammatory response to foreign bodies was not observed in the treated pigs, indicating its potential for clinical transition.

DISCUSSION
Here, we report the potential for an efficient miRNA delivery system that simultaneously integrates immune modification and angiogenesis enhancement in the field of MI therapy. This study demonstrates the efficacy and feasibility of a delivery system in a clinically relevant porcine MI model, where both the pathophysiology and the administration mimic what would be observed and performed in humans.

Current therapeutic strategies (angiogenic therapy or anti-inflammatory therapy) involving protein delivery or gene therapy for treating MI have limited success in reducing infarct size (*42*, *43*). The results of our study suggest that therapeutic outcome relies on both immunomodulation and angiogenesis. This study demonstrated that MSNs could reduce the inflammatory responses that can modify tissue remodeling and prevent fibrous tissue formation for improved repair after MI. Specifically, the effect of the resultant microenvironment can be further enhanced with sustained miR-21-5p delivery via MSNs and synergistically stimulate angiogenesis as well as changes in the morphology and pumping effectiveness of the heart after MI.

To date, the study to use miRNA for the treatment of ischemic cardiovascular disease in a preclinical pig model was performed by Gabisonia *et al.* (*22*). Gabisonia *et al.* used miR-199a therapy in an attempt to stimulate cardiomyocyte proliferation. The approach
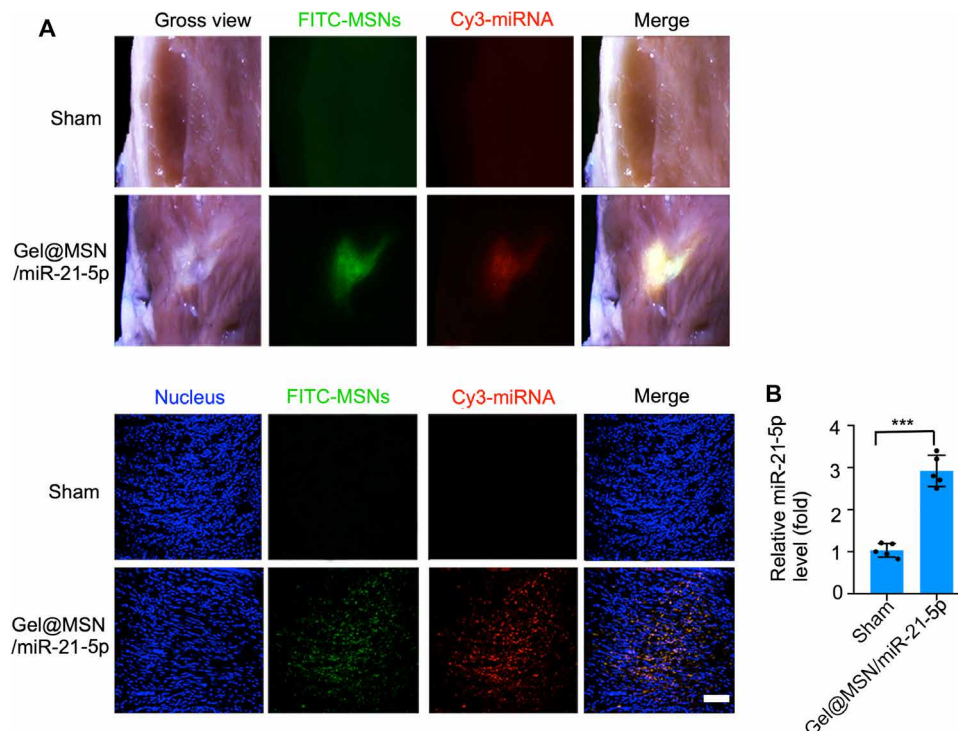
Fig. 8. The MSN/miRNA complex could only be released from Gel@MSN/miR-21-5p at the infarct region. For examination of on-demand delivery, the hearts were harvested at 28 days after MI for fluorescent imaging, RNA extraction, and real-time quantitative PCR analysis. (**A**) The fluorescent images showed that there were no transfecting cells detected in the sham group. In contrast, it showed that the area of FITC and Cy3 fluorescence exactly overlapped with the infarct region. (**B**) Quantification of miR-21-5p levels showed that the MSN/miRNA complex could be highly transfected into cells within the infarct region in vivo. Scale bar, 100 μm. ***$P < 0.01$. The data are shown as means ± SD. Photo credit: Yan Li, Shanghai Ninth People's Hospital, College of Stomatology, Shanghai Jiao Tong University School of Medicine, Shanghai 200011, China.

enabled the induction of preexisting cardiomyocytes to reenter the cell cycle and rebuild the injured heart (*44*). Substantial improvements in cardiac function and structure were attributed to this process. However, there are potential limitations of cardiomyocyte proliferation after birth including cardiomegaly or hypertrophy, as well as possible arrhythmias due to the immaturity of myocyte conduction or poor coupling with existing myocardium (*45*). As reported by Gabisonia, the generation of areas of poorly differentiated cardiomyocytes might cause tachyarrhythmias and eventually determine fatal reentry electric circuits. The adverse effects were also observed in several other studies, that long-term stimulation of cardiomyocyte proliferation might result in impaired cardiac function or arrhythmic events (*46–48*). In the current study, we attempted to use specific miR-21-5p–based therapies to promote angiogenesis in infarct areas, which may further facilitate rescuing resident cardiomyocytes in an injured heart. We focused on myocardial salvage rather than replacement. The proangiogenic effects of miR-21-5p were characterized with multiple in vitro and in vivo experiments and could be attributed to targeting SPRY1. Loss of SPRY1 leads to the expression of proangiogenic cytokines (VEGFA and PDGF-BB) in endothelial cells. While manipulation of proteins in the Hippo pathway (identified as miR-199a targets) promotes adult cardiomyocyte cell cycling, animals subjected to this type of treatment also exhibit cardiac dysfunction and heart failure in the long term (*47, 48*). Our strategy represents another direction to promote MI repair. Until now, no major case of arrhythmias has been reported to be associated with long-term proangiogenic therapies in either

animal studies or clinical trials. In addition, Gabisonia *et al.* used adeno-associated virus vectors as therapeutic and investigational tools, which have advantages such as high transfection efficiency. However, such virus-based delivery systems could lead to uncontrollable continuous miR-199a expression and unrestrained cardiac growth in the long term, which would eventually result in sudden death due to arrhythmia at weeks 7 to 8 in most of the treated pigs because controlled miRNA delivery was beyond the current capabilities of virus-mediated gene transfer. Therefore, the treatment needs to be carefully dosed, which could be achieved through the delivery of naked, synthetic miRNA mimics. In our study, a local on-demand and controlled delivery system was described. The system provided a controlled miR-21-5p mimic delivery, with ~75% release over 7 days at pH 6.8 in vitro. In addition, considering the limitation of current RNAi-based therapy associated with potential off-target accumulation, multiple works have been done in this area to optimize the RNAi delivery system (*16, 18, 19, 23*). For example, a hydrogel system used ultraviolet as the external stimulus to achieve on-demand controlled localized release of RNA at designated time points to induce human mesenchymal stem cell (hMSC) osteogenesis (*18, 19*). In the present study, the hydrogel is designed to be pH stimuli responsive to achieve on-demand miRNA delivery for persistent and accuracy therapeutic effect on MI. The miRNA delivery system (Gel@MSN/miR-21-5p) specifically released MSN/miR-21-5p only at the infarct region without affecting the surrounding healthy tissues, which addresses the safety issue associated with miRNA-based therapy. As shown in fig. S15, two
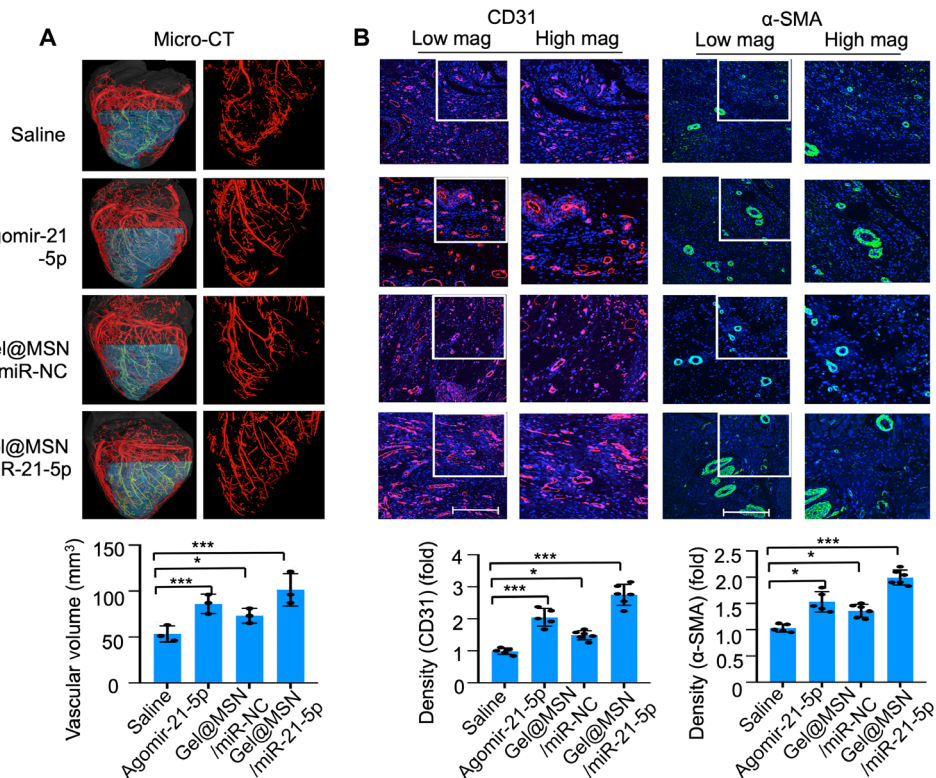
Fig. 9. Gel@MSN/miR-21-5p promoted local neovascularization at the infarct site after MI. (**A**) Micro-CT angiography analysis of 3D vascular structures within the infarct zone 28 days after MI indicates that the vascular volume was significantly increased in the Gel@MSN/miR-21-5p treatment group. The vascular volume within the infarct zone was quantitatively analyzed. *$P < 0.05$ and ***$P < 0.01$. $n = 3$ per group. (**B**) Immunofluorescence staining for CD31 (red) identified the vascular endothelium, and staining for α-SMA (green) identified myofibroblasts and pericytes, showing that the cardiac capillary density in histological sections of the healing infarct zone was significantly higher in the Gel@MSN/miR-21-5p treatment group than in the other groups. The CD31 and α-SMA staining intensities in the above-described groups were quantitatively analyzed (scale bars, 500 mm). *$P < 0.05$ and ***$P < 0.01$. Sham, $n = 3$; MI/saline, $n = 5$; MI/agomir, $n = 5$; MI/Gel@MSN/miR-NC, $n = 6$; and MI/Gel@MSN/miR-21-5p, $n = 6$. The data are shown as the means ± SD. Photo credit: Yan Li, Shanghai Ninth People's Hospital, College of Stomatology, Shanghai Jiao Tong University School of Medicine, Shanghai 200011, China.

pigs survived out to 11 months after Gel@MSN/miR-21 treatment, and electrocardiography (ECG) was performed. ECG analysis of Q wave and T wave showed that ECG signal at 11 months is similar to that at 4 weeks after Gel@MSN/miR-21 treatment, indicating that Gel@MSN/miR-21 was not likely to pose a long-term safety risk.

Acute inflammation caused by MI is a protective response that kills invading pathogens, should be self-limiting, and leads to healing (*49*). However, excess activation of the acute inflammatory response leads to cardiac myocyte death. Macrophages play a central role in regulating inflammation. Modulation of macrophage activation may contribute to the resolution of cardiac injury after MI. The results of this study indicate that MSNs can be used to inhibit proinflammatory polarization (M1) in an inflammatory microenvironment following ischemic muscle injury in vivo (*50*). Gulin-Sarfraz *et al.* (*13*) also noticed that empty mesoporous silica particles could reduce the number of neutrophils and down-modulate the inflammatory response in a mouse airway inflammation model. In addition, our data showed that MSNs modulated immune response through down-regulating TLR2, which inhibited the activation of NFκB signaling and subsequently decreased the release of proinflammatory cytokines (TNF-α, IL-1β, and IL-6). Our results are similar to the findings of Lee *et al.* (*51*), who demonstrated that exposure to MSNs decreased the expression of proinflammatory cytokines such as

TNF-α, IL-1β, and IL-6 in macrophages. Consistent with these results, a more recent study indicated that MSNs inhibit lymphocyte proliferation, suppress the killing activity of natural killer cells, and decrease proinflammatory cytokine and nitric oxide production in macrophage cells (*36*).

Previous studies have demonstrated that angiogenesis can be promoted by the fine-tuned delivery of multiple growth factors and cells with biomaterials (*52*, *53*). It relies on the precisely controlled sequential release or direct serial delivery, which are unfavorable for clinical use. The present study has provided a relatively simple approach that shows not only equivalent efficacy in promoting angiogenesis but also a modified cardiac inflammatory response in pigs after MI, suggesting that achieving cardiac repair through the stimulation of angiogenesis in the infarct region with a miRNA (miR-21-5p)–based strategy is attainable in large mammals. The vascular volume was significantly improved within the infarct region in pigs treated with Gel@MSN/miR-21-5p. The enhanced vessels within the infarct region were associated with the accumulation of endothelial cells (identified by CD31^{+}) and mural cells (identified by α-SMA^{+}) 28 days after MI. The mechanism by which miR-21-5p exerts its cardiac proangiogenic effects in the myocardium was also studied. KEGG analysis suggested that treatment with miR-21-5p complex was positively associated with key angiogenic signaling pathways
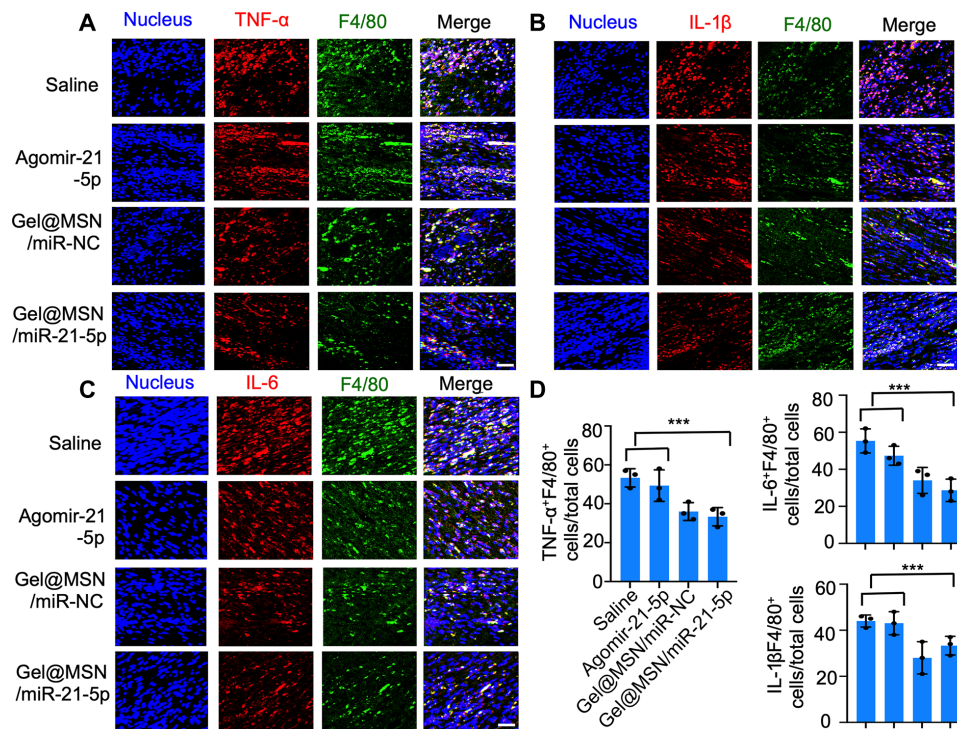
Fig. 10. Immunomodulatory effects of Gel@MSN/miR-21 on the infarct region at 1 day post MI in vivo. Histological sections of the infarct zone (day 1 after MI) were immuno-labeled with antibodies targeting TNF-α (A), IL-6 (B), or IL-1β (C) and colabeled with the macrophage marker F4/80 (green). Cell nuclei were counterstained with DAPI (blue). (**D**) The percentages of cells double positive for F4/80 and TNF-α, IL-1β, or IL-6 (TNF-α–, IL-1β–, or IL-6–expressing macrophages, respectively) were quantified. Quantification was performed in at least eight high-resolution images acquired from at least eight different regions of each heart. Scale bars, 100 μm. ***$P < 0.01$. $n = 3$ per group. The data are shown as the means ± SD. Photo credit: Yan Li, Shanghai Ninth People's Hospital, College of Stomatology, Shanghai Jiao Tong University School of Medicine, Shanghai 200011, China.

such as VEGF signaling and PDGF signaling. Multiple experiments were further conducted and concluded that the delivery of miR-21-5p promoted angiogenesis by targeting SPRY1 and subsequently activating VEGF-induced ERK-MAPK signaling. Together, these data suggest that endogenous cardiac repair may be facilitated by the miR-21-5p–induced angiogenic network.

Increasing reports have revealed the advantage and importance of biomaterials in cardiac tissue engineering. Despite the enthusiasm, there are relatively few ongoing clinical trials using injected materials for cardiac repair, perhaps due to a lack of evidence in large-animal studies, which are necessary before progressing to human trials. Pig models offer an alternative because of their anatomical and physiological similarities to humans. The use of a pig model of MI may provide valuable information regarding the safety and efficacy of therapeutic strategies for MI in clinic. We performed a large-animal study with a pig model to demonstrate the translational potential. However, because the immediate treatment after MI may not be relevant to clinical situations, whether this approach also works in chronic cases and whether there exists an optimal therapeutic time window require further evaluation. There are also human-specific issues to consider including PEG immunity and species-specific interactions. Thus, understanding the factors that affect PEG immunity is crucial for both researchers and clinicians to ensure the treatment safety in clinic. Optimization of Gel@MSN/miR-21-5p dose and long-term studies are also needed for clinical translation.

In summary, the two-stage gene delivery system Gel@MSN/miR-21-5p developed in this study consists of three key components, pH-responsive hydrogel matrix, MSNs, and miR-21-5p. The responsive hydrogel serves as a matrix to achieve a highly localized

drug release triggered by an acidic microenvironment and a 1-week sustained drug release (first stage release); MSN is the gene transfection vector (second stage release) and itself alone also resolves early inflammation by suppressing the TLR/NFκB signaling pathway; and miR-21-5p promotes angiogenesis and mature vessel formation by targeting SPRY1 and subsequently activating VEGF-induced ERK-MAPK signaling. The synergy among these three elements demonstrated significance in treating MI in a swine model via a combination of anti-inflammatory and proangiogenic effects. Clinically relevant positive outcomes were observed upon Gel@MSN/miR-21-5p treatment, such as improved cardiac remodeling, reduced fibrosis formation and infarct size, and increased vascularization. The injectable property of Gel@MSN/miR-21-5p makes it potentially translatable to minimally invasive transcatheter-based surgery. In addition, this study is a proof of concept for controlled gene delivery and can serve as a technological platform to better elucidate the dose-dependent response of genes in MI treatment or deliver any other nucleic acids (such as DNAs, mRNAs, siRNAs, and miRNAs) or treat any other disease.

MATERIALS AND METHODS
Study design

The purpose of this study was to design a controlled on-demand miR-21-5p delivery system (Gel@MSN/miR-21-5p) using MSNs combined with a hydrogel matrix, simultaneously integrating immune modification and angiogenesis enhancement in the field of MI therapy. Gel@MSN/miR-21-5p was fabricated by embedding

MSN/miR-21-5p complexes into an injectable hydrogel matrix. We performed studies to determine the mechanical properties, structure, and on-demand release profile of Gel@MSN/miR-21-5p.

For the in vitro experiment, real-time quantitative PCR, Western blot, and enzyme-linked immunosorbent assay (ELISA) were performed to assess the immunomodulatory effect of MSNs. Real-time quantitative PCR, Western blot, ELISA, and tube formation assays were performed to determine the proangiogenic effect of miR-21-5p. The mechanisms underlying MSN-mediated inflammatory effects and miR-21-5p–mediated proangiogenic effects were studied by proteogenomic analysis, real-time quantitative PCR, and Western blot.

For the in vivo experiments, pigs were randomly assigned to treatment groups, and, wherever applicable, treatment conditions were kept blinded until statistical analysis. Group sizes of at least five animals were chosen, which indicated that the therapeutic efficacy and safety of the Gel@MSN/miR-21-5p could be robustly identified. MI was characterized using multiple methods including echocardiography, delayed enhancement CT, TTC staining, and histological examination. The potential cardiac-protective effect against apoptosis induced by ischemia was analyzed by immunofluorescence analysis. The duration and efficiency of MSNs and miRNA delivered by Gel@MSN/miR-21-5p injection were monitored using time course analysis.

Animal studies
Animal protocols related to this study were reviewed and approved by the Institutional Animal Care and Use Committee at the School of Medicine of Shanghai Jiao Tong University. All experiments were performed in accordance with the guidelines published by the Institutional Animal Care and Use Committee at the School of Medicine of Shanghai Jiao Tong University, Shanghai. All animals were obtained from the Ninth People's Hospital Animal Center (Shanghai, China).

MI model and treatment administration
Yucatan mini pigs (male, 45 to 50 kg) were anesthetized with tiletamine hydrochloride and zolazepam hydrochloride (4 mg/kg). To establish the porcine MI model, transthoracic 2D echocardiographic measurement by Simpson's method (S5-1 transducer, PHILIPS Medical Systems) was performed to ensure that the animal was healthy before instrumentation and MI induction. Following baseline echocardiographic measurements, light anesthesia was maintained by continuous intravenous infusion of propofol (30 to 40 μg kg^{-1} min^{-1}). ECG, heart rate, and arterial pressure were constantly monitored. The pericardium was opened through a left thoracotomy, and the first two obtuse marginal arteries of the circumflex artery (OM1 and OM2) were identified and ligated to induce MI. Past studies demonstrated that this technique creates a uniform and consistent MI (24). The pericardium was left open. Pigs were randomized to receive a total of six distinct injection of saline, agomiR-21-5p, Gel@MSN/miR-NC, or Gel@MSN/miR-21-5p within a targeted 2 × 2 cm region of mid-myocardium immediately after MI (six injection sites, 100 μl per injection). Sham controls were was processed in an identical fashion with the exception of coronary artery ligation. The injection of each target site is shown in fig. S13. For the Gel@MSN/miR-NC and Gel@MSN/miR-21 treatments, the miR-NC or miR-21 was preloaded in the MSN-NH₂-TMA with a mass ratio of 1:10 between miRNA/MSNs. Then, the sterilized aqueous solutions (600 μl) containing RNA-loaded MSN-NH2-TMA,

CHO-PEG-CHO, and α-CD with a mass ratio of 1:5:5 were incubated for 5 min to form an injectable hydrogel precursor with weak interaction, which was further drawn into a separate syringe, and injected into the mid-myocardium to form the final hydrogel at the target site immediately following MI induction. Animals were carefully monitored until they fully recovered from anesthesia.

Echocardiography measurement
Pigs were sedated at baseline, and 2D echocardiographic measurements by Simpson's method (IE33 digital ultrasonic scanner, PHILIPS Medical Systems, USA) were performed in right lateral recumbency. Echocardiography measurements were taken before surgery (baseline) and at 45 min, 14 days, and 28 days following MI. Transthoracic echocardiography allowed assessment and further calculation of LV dimensions, cardiac chamber size, wall thicknesses, EF, LVEDV, and LVEDd according to the biplane modified Simpson's rule. For these measurements, standard parasternal long-axis and apical chamber views were obtained.

LV assessment with CT
CT examinations were performed at 28 days after MI. Animals were sedated with a cocktail injection of tiletamine hydrochloride (4 mg/kg) and zolazepam hydrochloride (4 mg/kg) injection. Pigs were placed in a right lateral position.

CT images were acquired with a clinical 320-slice scanner (Aquilion One, TOSHIBA Medical Systems). The heart was scanned along two long-axis views (vertical and horizontal) and with one set of short-axis views covering the entire LV from the atrioventricular valve plane to the apex. The following parameters were used: a tube voltage of 100 kV, a tube current of 75 mA, a gantry rotation time of 330 ms, 0.5-mm section thickness, a resolution of 0.5 × 0.5 mm, and free breathing. The CT contrast medium (Ultravist 370, Schering) was injected at a flow rate of 3.5 ml/s. To identify the scar and quantify the extent of post-infarction fibrosis, delayed contrast-enhanced multidetector CT images were acquired to assess viability 3 to 5 min after the administration of contrast media for LV function.

Multiphase reconstruction was performed with commercially available software (VITAL, TOSHIBA Medical Systems, Japan) by using short-axis slices from the base of the heart to the apex. The end diastole and end systole were defined as the maximal and minimal LV volume, respectively.

Micro-CT angiography
The hearts from each group were harvested, and blood vessels within the heart were imaged by angiography, as previously described (54). Briefly, a 50.8-millimeter, 18-gauge catheter (Surflo Teflon IV Catheter, Terumo Medical, USA) was inserted into the left ventricle of the heart and advanced into the ascending aorta. A 0.9% normal saline solution containing heparin sodium (100 U/ml) was perfused through the vasculature. The vasculature was then fixed by perfusion with 10% neutral buffered formalin (NBF) and cleared with saline. Last, 25 ml of polymerizable, lead chromate–based, radiopaque contrast agent (Microfil MV-122, Flow Tech, USA) was injected using a 30-ml syringe. Samples were stored at 4°C for 24 hours to allow polymerization of the contrast agent.

Samples were scanned using micro-CT (Y. Cheetah, YXLON, Germany) with the following settings: 90 kV, 50 μA source current, exposure time of 907 ms, and two images every 0.5° of a 360° rotation range at a voxel size of 76 μm. 3D reconstruction of the micro-CT

image was completed and analyzed using the manufacturer's evaluation software (VG studiomax 3.0). The reconstruction was performed using binning mode, providing an isotropic voxel size of 76 μm.

Since the infarct area is clearly visible in the heart tissue slice, matching the micro-CT image slices with their corresponding tissue slices could identify the infarct zone within the 3D micro-CT reconstructed model. The sectioning planes of the microtomograph and of the tissue samples are parallel. After sectioning, the infarct areas (infarcted myocardium appears pale) of the heart tissue slices were counterstained in red. After obtaining micro-CT images, the infarct areas of the micro-CT images were identified on the basis of the observation of the tissue slices.

TTC staining

The heart tissue was sectioned starting from the base to the apex. After sectioning, slices were immediately immersed in 2% TTC in 0.9% NaCl at 37°C for 30 min for vital staining. Infarcted myocardium appeared pale after TTC staining. The MI area (TTC negative, white) is outlined. The infarcted area and the total area of the LV wall were analyzed using ImageJ software. The infarct size was calculated as follows: counts of TTC-negative area/counts of total LV wall area (%) on short-axial middle LV myocardial slices.

Histology analysis

The excised hearts were sectioned through four horizontal planes, and each section was then subdivided into subsections for further histological and molecular analyses, as shown in fig. S14. Briefly, each heart was sectioned into four 1-cm-thick slices, starting from the apex toward the base. Then, two regions (indicated by letters) of each slice were chosen for further histological and molecular analyses. In all quantifications, we considered eight sectors of the four heart sections, and the same regions were chosen in animals with different treatments.

Pig hearts were carefully harvested 28 days following infarction. Samples representing the mid-infarct were sliced. These tissue samples were routinely processed for histologic analysis, and sections (5 μm thick) were stained with hematoxylin and eosin (H&E) and Masson's trichrome, as previously described (55). Capillary densities were examined by counting the number of capillaries stained with anti-CD31 (ab28364, Abcam, USA) and anti-SMA (ab5694, Abcam, USA) antibodies. For hydrogel immunomodulatory investigation, hearts were collected and processed after 1 and 28 days after MI. Immunofluorescence was used as previously described to identify F4/80^{+} cells (ab6640, Abcam, USA) colabeling with anti–TNF-α (ab6671, Abcam, USA), anti–IL-6 (ab6672, Abcam, USA), or anti–IL-1β antibody (NB600-633, Novas, USA); Alexa Fluor 488–labeled donkey anti-rat antibody (Jackson ImmunoResearch Laboratories, USA) and the Alexa Fluor 594–labeled anti-rabbit antibody (Jackson ImmunoResearch Laboratories, USA) were used for visualization. Slides were counterstained with DAPI (56). Immunohistochemistry was used to verify cardiomyocytes with anti–cardiac troponin-T antibody (ab10214). ImageJ software was applied to count blue pixels (positive for collagen) within that region in the trichrome images.

Time course analysis of transfection efficiency of Gel@MSN/miR-21-5p was performed in vivo. MSNs were prelabeled with FITC (green), or miR-21-5p was prelabeled with Cy3 (red). The hydrogel (FITC-labeled Gel@MSN/miR-21-5p or Cy3-labeled Gel@MSN/miR-21-5p) was injected into the mid-myocardium of each target site

of pigs. The delivery efficiency of miR-21-5p into endothelial cells was examined by identifying CD31^{+} cells (ab28364, Abcam, USA) co-labeling with Cy3-labeled miR-21-5p. The delivery efficiency of MSNs into macrophages was examined by identifying F4/80^{+} cells (ab6640, Abcam, USA) colabeled with FITC-labeled MSNs.

To assess whether MSNs could protect against apoptosis in cardiomyocytes, a terminal deoxynucleotidyl transferase–mediated deoxyuridine triphosphate nick end labeling assay using an In Situ Cell Death Detection Kit (Roche, Switzerland) was performed at an earlier time (1 day) after MI, which labels broken DNA strands that are often associated with apoptosis. Percentages of positively stained cells were determined by counting the numbers of labeled cells and total cells.

Primary cell isolation and cell culture

The macrophage activation state was evaluated after intraperitoneal injections of LPS (Sigma-Aldrich, St. Louis, MO; 250 μg in 0.5 ml of saline) into mice. Primary peritoneal macrophages were obtained from 20 g of female C57BL6J mice, as previously described (57). Briefly, cell lavage was collected by flushing the peritoneum with cold PBS. The peritoneum was centrifuged (800g, 4°C, 9 min), and the pellet was incubated with ACK buffer (Fisher Scientific, Chino, USA) for 1 min to lyse erythrocytes. The remaining cells were cultured in RPMI 1640 medium and 10% fetal bovine serum (FBS) (Gibco, Gaithersburg, USA) at 37°C in a 5% CO_2 atmosphere and plated to select for adherent macrophages.

Primary cardiomyocytes were obtained from adult C57BL6J mice (8 weeks), as previously described (58). Briefly, the animal is euthanized humanely by cervical dislocation, and the heart is excised, taking care to remove the pericardium. Blood is removed from the coronary vessels after adequate perfusion with EDTA. Next, the heart is perfused with enzyme solution for 8 to 14 min. At the end of the enzyme digestion, the enzyme solution is flushed with 100 μM Ca solution for 5 min, after which the heart is excised by dissecting the cannula, atria, and aorta. Once the first digestion was completed, the heart was transferred to a sterile petri dish and a second digestion step is carried out. The ventricular tissue is chopped with small scissors. Fresh digestion buffer was added, and the heart was quickly triturated with fine tweezers and forceps. This second digestion was performed at 37°C in an incubator with 5% CO_2 for 10 min to facilitate the collagenase activity. The reaction was halted by adding stop buffer containing FBS (Gibco), and the sample was filtered through a 100-μm mesh. Following this, cardiomyocytes were purified via gravity separation in a falcon tube for 15 min and washed with Ca solution. After purification, cells were counted in a hemocytometer, seeded in laminin-coated culture dishes, and placed in an incubator with 5% CO_2 at 37°C.

Endothelial cells were purchased from the cell and stem cell bank (GNO 15, Chinese Academy of Sciences, China) and were maintained in culture with Dulbecco's modified Eagle's medium (DMEM) (Gibco) supplied with 10% FBS (BioInd, Israel), as detailed by the manufacturer.

The tube formation assay was performed as previously described (59). Briefly, growth factor–reduced Matrigel matrix (Life Technology) was plated in a 24-well plate after thawing at 4°C overnight. The plate was then incubated at 37°C for 30 min to allow the Matrigel to polymerize. MSNs, MSN/miRNA-NC, and MSN/miRNA-21–transfected calcein-labeled endothelial cells in endothelial basal medium 2 (EBM2) supplemented with 0.5% FBS and basic fibroblast

growth factor (5 ng/ml) (FGF) final were seeded on the Matrigel-coated well. The plate was then incubated at 37°C in a 5% CO_2 humidified atmosphere. Tube formation was observed at 8 and 16 hours with confocal microscopy. The tube formation ability was determined by measuring the total tube length of endothelial cells with ImageJ software.

Flow cytometric assay

For flow cytometric analyses, cells were blocked with 10% FBS for 10 min on ice and subsequently stained with fluorochrome-tagged anti-F4/80 (BM8, BioLegend) or APC-labeled anti-CD31 (eBioscience, 17-0319-42). All stains were performed in 1% bovine serum albumin PBS buffer for 1 hour in the dark at 4°C, followed by two washing steps. Samples were analyzed on a FACSCalibur (BD Biosciences, USA). Dead cells were excluded by forward and side scatter, and data analysis was performed using FlowJo software version 7.6.3 (Tree Star Inc., Ashland, USA).

MSN uptake analysis

For in vitro uptake analysis, isolated peritoneal macrophages were cocultured with FITC-labeled nanoparticles (100 μg/ml). For in vivo uptake analysis, FITC-labeled Gel@MSN/miR-21-5p was injected into the mid-myocardium of the pig's heart. In vitro and in vivo quantitative uptake of the MSNs by macrophages was determined by quantifying the fluorescence intensity of cells that were positive for F4/80 (ab6640, Abcam, USA) and showed colocalization with FITC.

Ischemia and hypoxia exposure

The growth medium of the hypoxic/ischemia group was replaced with serum-free DMEM. Cells were placed in a hypoxic incubator (Sanyo, O_2/CO_2 incubator MCO-18M) with oxygen adjusted to 1.0% and CO_2 adjusted to 5%. Normal culture (regular medium under 21% oxygen and 5% CO_2) served as a control.

RNA extraction and real-time quantitative PCR

The hearts of pigs were collected. Total miRNA from the collected cells or the heart was extracted using the RNeasy Mini Kit (Qiagen) according to the manufacturer's instructions. For miRNA level detection, reverse transcription was performed using the Reverse Transcription kit (Takara RR037a, USA) with miRNA-specific stem-loop RT primer (ID: miR8001313, RiboBio, China). Reverse transcriptase reactions contained 0.5 μg of RNA samples, 0.2 μM stem-loop RT primer, 1× RT buffer, 50 pmol of random primers 6, and PrimerScript Reverse Transcriptase (200 U·μl^{-1}). The 10-μl reactions were incubated in a T100 thermal cycler (Bio-Rad, Hercules, USA) for 15 min at 37°C, 5 s at 72°C, and then held at 4°C. One microliter of cDNA was PCR-amplified using Premix Taq (Takara RR902A) with 1 μl of forward primer (0.2 μM) and 1 μl of reverse primer (0.2 μM) for miR-21-5p (RiboBio, ID: miR8001314). The 25-μl reaction volume consisted of 1 μl of cDNA, 12.5 μl of Premix Taq, 9.5 μl of ddH$_2$O, 1 μl of forward primer (0.2 μM), and 1 μl of reverse primer (0.2 μM). The reactions were performed on a T100 thermal cycler.

The cDNAs were diluted 10 times to perform real-time quantitative PCR using TB Green Premix Ex Taq (Takara RR420A) for miR-21-5p level detection. The 25-μl reaction volume consisted of 1 μl of cDNA, 12.5 μl of Green Premix Ex Taq, 9.5 μl of ddH$_2$O, 1 μl of forward primer (0.4 μM), and 1 μl of reverse primer (0.4 μM) for miR-21-5p (RiboBio, ID: miR8001314).

For miRNA level detection, cDNAs were synthesized using a reverse transcription kit (Takara, RR037a). Reverse transcriptase reactions contained 0.5 μg of RNA samples, 25 pmol of Oligo dT Primer, 1× RT buffer, 50 pmol of random six primers, and PrimerScript Reverse Transcriptase (200 U·μl^{-1}). The 10-μl reactions were incubated in a MyCycler thermal cycler (Bio-Rad, Hercules, CA) for 15 min at 37°C and 5 s at 72°C and then held at 4°C. The cDNAs were then diluted 10 times to perform real-time quantitative PCR for expression confirmation and expression pattern analysis.

The primers used are as follows: β-actin (5′-CAGGATTCCAT-ACCCAAGAAG-3′ and 5′-AACCCTAAGGCCAACCGTG-3′), IL-1β (5′-GAAATGCCACCTTTTGACAGTG-3′ and 5′-TGGAT-GCTCTCATCAGGACAG-3′), TNF-α (5′-GACGTGGAACTGG-CAGAAGAG-3′ and 5′-TTGGTGGTTTGTGAGTGTGAG-3′), IL-6 (5′-TCTATACCACTTCACAAGTCGGA-3′ and 5′-GAAT-TGCCATTGCACAACTCTTT-3′), TLR1 (5′-CCGTCCCAAG-TTAGCCCATT-3′ and 5′-TCCCCCATCGCTGTACCTTA-3′), TLR2 (5′-TGCGGACTGTTTCCTTCTGA-3′ and 5′-GCGTTTG-CTGAAGAGGACTG-3′), TLR3 (5′-TACAAAGTTGGGAACGGG-GG-3′ and 5′-GGTTCAGTTGGGCGTTGTTC-3′), and TLR8 (5′-ACAAACGTTTTACCTTCCTTTGTC-3′ and 5′-ATG-CAGTTGACGATGGTTGC-3′).

Western blot analysis

Western blotting was performed as previously described (56). Total protein was extracted using the EpiQuik whole-cell extraction kit (Epigentek, USA). The protein concentration was measured following the manufacturer's instructions (Bio-Rad, USA). Protein was applied to and separated on 4 to 15% NuPAGE gels (Bio-Rad) and transferred to polyvinylidene difluoride membranes (Millipore, USA). The membranes were blocked with 5% bovine serum albumin and incubated with specific primary antibodies against the following: TNF-α (AF-410-NA, R&D, USA), IL-1β (Novus, AF-401-NA), IL-6 (bs-0782R, Bioss, USA), VEGFA (DF7470, Affinity, USA), PDGF-BB (bs-1316R, Bioss), TLR1 (NB100-56563, Novus), TLR2 (Abcam, ab209217), TLR3 (NBP2-24875, Novus), TLR8 (NBP2-24917, Novus), NFκB (CST8242s, Cell Signaling Technology, USA), p-NFκB (CST3033s), SPRY1 (Abcam, ab111523), P-ERK1/2 (AF1018, R&D), ERK1/2 (AF1576, R&D), P-AKT (AF887, R&D), AKT (MAB2055, R&D), P-FAK (MAB4528, R&D), FAK (AF4467, R&D), P-P38 (CST4511), P38 (CST8690), and GAPDH (ab181602) at a ratio of 1:1000 overnight.

Horseradish peroxidase–conjugated IgG (1:10,000 dilution) from Santa Cruz Biotechnology (Santa Cruz, USA) was incubated with the membrane for 1 hour, after which the membranes were enhanced with a SuperSignal West Pico Chemiluminescent Substrate (Thermo Fisher Scientific, USA). The relative amounts of the transferred proteins were quantified by scanning the autoradiographic films. Total protein or nuclear protein was normalized to the corresponding β-actin.

Enzyme-linked immunosorbent assay

For VEGFA and PDGF-BB protein secretion analysis, cells were pretreated with MSN complex loaded with 5 nmol of miR-21-5p as described above. After 6 hours of culture, the medium was replaced with fresh growth medium supplemented with 5.0% serum substitute Nu-Serum (NuS, BD, USA). Samples were collected at 48 hours. VEGFA and PDGF-BB protein levels in the medium were determined using an ELISA according to the manufacturer's instructions

(R&D Corp., USA). Absorbance was measured at 450 nm with a microplate reader (MTP-800Lab, Corona Electric, Japan). A standard curve was plotted to determine the VEGFA and PDGF-BB concentrations. The values are expressed as picograms per milliliter.

In vivo hydrogel degradation analysis

To detect the degradation of Gel@MSN/miR-21 in vivo, the PEG frame of the hydrogel was labeled rhodamine B. Sixty microliters of Gel@MSN/miR-21 was injected into the mid-myocardium of rats after induction of MI. To monitor the residual MSNs in vivo, 60 μl of hydrogel containing rhodamine B–labeled MSNs was injected into the mid-myocardium of rats after induction of MI. At the indicated time points, rats were euthanized, and the hearts were removed from the animals. The organs were entirely maintained on ice until ex vivo analysis with Xenogen IVIS imaging system (Alameda, USA). Epifluorescence images of the hearts were acquired. Captured images were then analyzed using the Living Image 4.3.1 software (PerkinElmer Inc., USA). All data obtained by Xenogen IVIS were expressed as radiant efficiency, were assumed to be a calibrated measurement of the photon emission from the subject, and were technically defined as fluorescence emission radiance per incident excitation intensity as follows: photons/s/cm^2/sr.

Statistical analyses

All numerical data are presented as the means ± SD. Statistical analysis was performed using commercially available software (SPSS 26). Data were first checked for normal distribution, and differences among groups were compared by one-way analysis of variance (ANOVA) followed by the Bonferroni post hoc test. Comparisons between two groups were made using the unpaired t test. For all statistical analyses, significance was accepted at $P < 0.05$.

SUPPLEMENTARY MATERIALS

Supplementary material for this article is available at http://advances.sciencemag.org/cgi/content/full/7/9/eabd6740/DC1

View/request a protocol for this paper from *Bio-protocol*.

REFERENCES AND NOTES

1. C. Nathan, Points of control in inflammation. *Nature* **420**, 846–852 (2002).
2. I. Bytyci, G. Bajraktari, Mortality in heart failure patients. *Anatol. J. Cardiol.* **15**, 63–68 (2015).
3. C. Cochain, K. M. Channon, J. S. Silvestre, Angiogenesis in the infarcted myocardium. *Antioxid. Redox Signal.* **18**, 1100–1113 (2013).
4. D. Orlic, J. Kajstura, S. Chimenti, F. Limana, I. Jakoniuk, F. Quaini, B. Nadal-Ginard, D. M. Bodine, A. Leri, P. Anversa, Mobilized bone marrow cells repair the infarcted heart, improving function and survival. *Proc. Natl. Acad. Sci. U.S.A.* **98**, 10344–10349 (2001).
5. C. E. Murry, M. H. Soonpaa, H. Reinecke, H. Nakajima, H. O. Nakajima, M. Rubart, K. B. Pasumarthi, J. I. Virag, S. H. Bartelmez, V. Poppa, G. Bradford, J. D. Dowell, D. A. Williams, L. J. Field, Haematopoietic stem cells do not transdifferentiate into cardiac myocytes in myocardial infarcts. *Nature* **428**, 664–668 (2004).
6. B. Liu, B. W. Lee, K. Nakanishi, A. Villasante, R. Williamson, J. Metz, J. Kim, M. Kanai, L. Bi, K. Brown, G. Di Paolo, S. Homma, P. A. Sims, V. K. Topkara, G. Vunjak-Novakovic, Cardiac recovery via extended cell-free delivery of extracellular vesicles secreted by cardiomyocytes derived from induced pluripotent stem cells. *Nat. Biomed. Eng.* **2**, 293–303 (2018).
7. M. T. K. Zaldivia, J. D. McFadyen, B. Lim, X. Wang, K. Peter, Platelet-derived microvesicles in cardiovascular diseases. *Front Cardiovasc Med* **4**, 74 (2017).
8. A. Eulalio, M. Mano, M. Dal Ferro, L. Zentilin, G. Sinagra, S. Zacchigna, M. Giacca, Functional screening identifies miRNAs inducing cardiac regeneration. *Nature* **492**, 376–381 (2012).
9. L. Poliseno, A. Tuccoli, L. Mariani, M. Evangelista, L. Citti, K. Woods, A. Mercatanti, S. Hammond, G. Rainaldi, MicroRNAs modulate the angiogenic properties of HUVECs. *Blood* **108**, 3068–3071 (2006).
10. I. M. Verma, Medicine. Gene therapy that works. *Science* **341**, 853–855 (2013).
11. T. Harel-Adar, T. Ben Mordechai, Y. Amsalem, M. S. Feinberg, J. Leor, S. Cohen, Modulation of cardiac macrophages by phosphatidylserine-presenting liposomes improves infarct repair. *Proc. Natl. Acad. Sci. U.S.A.* **108**, 1827–1832 (2011).
12. E. Bracho-Sanchez, C. Q. Xia, M. J. Clare-Salzler, B. G. Keselowsky, Micro and nano material carriers for immunomodulation. *Am. J. Transplant.* **16**, 3362–3370 (2016).
13. T. Gulin-Sarfraz, S. Jonasson, E. Wigenstam, E. von Haartman, A. Bucht, J. M. Rosenholm, Feasibility study of mesoporous silica particles for pulmonary drug delivery: Therapeutic treatment with dexamethasone in a mouse model of airway inflammation. *Pharmaceutics* **11**, 149 (2019).
14. S. Fogli, C. Montis, S. Paccosi, A. Silvano, E. Michelucci, D. Berti, A. Bosi, A. Parenti, P. Romagnoli, Inorganic nanoparticles as potential regulators of immune response in dendritic cells. *Nanomedicine* **12**, 1647–1660 (2017).
15. D. W. Malcolm, Y. Wang, C. Overby, M. Newman, D. S. W. Benoit, Delivery of RNAi-based therapeutics for bone regeneration. *Curr. Osteoporos. Rep.* **18**, 312–324 (2020).
16. C. E. Nelson, M. K. Gupta, E. J. Adolph, S. A. Guelcher, C. L. Duvall, siRNA delivery from an injectable scaffold for wound therapy. *Adv. Wound Care* **2**, 93–99 (2013).
17. S. M. Sarett, C. E. Nelson, C. L. Duvall, Technologies for controlled, local delivery of siRNA. *J. Control. Release* **218**, 94–113 (2015).
18. C. T. Huynh, M. K. Nguyen, M. Naris, G. Y. Tonga, V. M. Rotello, E. Alsberg, Light-triggered RNA release and induction of hMSC osteogenesis via photodegradable, dual-crosslinked hydrogels. *Nanomedicine* **11**, 1535–1550 (2016).
19. C. T. Huynh, M. K. Nguyen, G. Y. Tonga, L. Longe, V. M. Rotello, E. Alsberg, Photocleavable hydrogels for light-triggered siRNA release. *Adv. Healthc. Mater.* **5**, 305–310 (2016).
20. M. K. Nguyen, O. Jeon, P. N. Dang, C. T. Huynh, D. Varghai, H. Riazi, A. McMillan, S. Herberg, E. Alsberg, RNA interfering molecule delivery from in situ forming biodegradable hydrogels for enhancement of bone formation in rat calvarial bone defects. *Acta Biomater.* **75**, 105–114 (2018).
21. Y. Wang, M. R. Newman, D. S. W. Benoit, Development of controlled drug delivery systems for bone fracture-targeted therapeutic delivery: A review. *Eur. J. Pharm. Biopharm.* **127**, 223–236 (2018).
22. K. Gabisonia, G. Prosdocimo, G. D. Aquaro, L. Carlucci, L. Zentilin, I. Secco, H. Ali, L. Braga, N. Gorgodze, F. Bernini, MicroRNA therapy stimulates uncontrolled cardiac repair after myocardial infarction in pigs. *Nature* **569**, 418–422 (2019).
23. M. D. Krebs, E. Alsberg, Localized, targeted, and sustained siRNA delivery. *Chemistry* **17**, 3054–3062 (2011).
24. B. P. Purcell, D. Lobb, M. B. Charati, S. M. Dorsey, R. J. Wade, K. N. Zellars, H. Doviak, S. Pettaway, C. B. Logdon, J. A. Shuman, P. D. Freels, J. H. Gorman 3rd, R. C. Gorman, F. G. Spinale, J. A. Burdick, Injectable and bioresponsive hydrogels for on-demand matrix metalloproteinase inhibition. *Nat. Mater.* **13**, 653–661 (2014).
25. L. L. Wang, Y. Liu, J. J. Chung, T. Wang, A. C. Gaffey, M. Lu, C. A. Cavanaugh, S. Zhou, R. Kanade, P. Atluri, E. E. Morrisey, J. A. Burdick, Local and sustained miRNA delivery from an injectable hydrogel promotes cardiomyocyte proliferation and functional regeneration after ischemic injury. *Nat Biomed Eng* **1**, 983–992 (2017).
26. J. A. Broderick, P. D. Zamore, MicroRNA therapeutics. *Gene Ther.* **18**, 1104–1110 (2011).
27. X. Liu, X. Chen, M. X. Chua, Z. Li, X. J. Loh, Y. L. Wu, Injectable supramolecular hydrogels as delivery agents of Bcl-2 conversion gene for the effective shrinkage of therapeutic resistance tumors. *Adv. Healthc. Mater.* **6**, 10.1002/adhm.201700159, (2017).
28. X. Guan, Z. Guo, L. Lin, J. Chen, H. Tian, X. Chen, Ultrasensitive pH triggered charge/size dual-rebound gene delivery system. *Nano Lett.* **16**, 6823–6831 (2016).
29. Q. Lei, S. B. Wang, J. J. Hu, Y. X. Lin, C. H. Zhu, L. Rong, X. Z. Zhang, Stimuli-responsive "Cluster Bomb" for programmed tumor therapy. *ACS Nano* **11**, 7201–7214 (2017).
30. D. J. Kumbhani, N. A. Healey, V. Birjiniuk, M. D. Crittenden, M. Josa, P. R. Treanor, S. F. Khuri, Determinants of regional myocardial acidosis during cardiac surgery. *Surgery* **136**, 190–198 (2004).
31. J. C. Garbern, E. Minami, P. S. Stayton, C. E. Murry, Delivery of basic fibroblast growth factor with a pH-responsive, injectable hydrogel to improve angiogenesis in infarcted myocardium. *Biomaterials* **32**, 2407–2416 (2011).
32. M. Dominska, D. M. Dykxhoorn, Breaking down the barriers: siRNA delivery and endosome escape. *J. Cell Sci.* **123**, 1183–1189 (2010).
33. E. Gaudio, B. Barbaro, D. Alvaro, S. Glaser, H. Francis, A. Franchitto, P. Onori, Y. Ueno, M. Marzioni, G. Fava, J. Venter, R. Reichenbach, R. Summers, G. Alpini, Administration of r-VEGF-A prevents hepatic artery ligation-induced bile duct damage in bile duct ligated rats. *Am. J. Physiol. Gastrointest. Liver Physiol.* **291**, G307–G317 (2006).
34. P. C. Hsieh, M. E. Davis, J. Gannon, C. MacGillivray, R. T. Lee, Controlled delivery of PDGF-BB for myocardial protection using injectable self-assembling peptide nanofibers. *J. Clin. Invest.* **116**, 237–248 (2006).
35. M. M. Tucureanu, D. Rebleanu, C. A. Constantinescu, M. Deleanu, G. Voicu, E. Butoi, M. Calin, I. Manduteanu, Lipopolysaccharide-induced inflammation in monocytes/macrophages is blocked by liposomal delivery of Gi-protein inhibitor. *Int. J. Nanomedicine* **13**, 63–76 (2018).

36. J. H. Kim, C. S. Kim, R. M. Ignacio, D. H. Kim, M. E. Sajo, E. H. Maeng, X. F. Qi, S. E. Park, Y. R. Kim, M. K. Kim, K. J. Lee, S. K. Kim, Immunotoxicity of silicon dioxide nanoparticles with different sizes and electrostatic charge. *Int. J. Nanomedicine* **9** (**Suppl 2**), 183–193 (2014).

37. L. Chen, J. Liu, Y. Zhang, G. Zhang, Y. Kang, A. Chen, X. Feng, L. Shao, The toxicity of silica nanoparticles to the immune system. *Nanomedicine* **13**, 1939–1962 (2018).

38. Y. Feng, S. Yang, Y. Ma, X. Y. Bai, X. Chen, Role of Toll-like receptors in diabetic renal lesions in a miniature pig model. *Sci. Adv.* **1**, e1400183 (2015).

39. P. Hari, F. R. Millar, N. Tarrats, J. Birch, A. Quintanilla, C. J. Rink, I. Fernandez-Duran, M. Muir, A. J. Finch, V. G. Brunton, J. F. Passos, J. P. Morton, L. Boulter, J. C. Acosta, The innate immune sensor Toll-like receptor 2 controls the senescence-associated secretory phenotype. *Sci. Adv.* **5**, eaaw0254 (2019).

40. A. Bassols, C. Costa, P. D. Eckersall, J. Osada, J. Sabria, J. Tibau, The pig as an animal model for human pathologies: A proteomics perspective. *Proteomics Clin. Appl.* **8**, 715–731 (2014).

41. A. Spannbauer, D. Traxler, K. Zlabinger, A. Gugerell, J. Winkler, J. Mester-Tonczar, D. Lukovic, C. Muller, M. Riesenhuber, N. Pavo, M. Gyongyosi, Large animal models of heart failure with reduced ejection fraction (HFrEF). *Front. Cardiovasc. Med.* **6**, 117 (2019).

42. M. A. Renault, D. W. Losordo, Therapeutic myocardial angiogenesis. *Microvasc. Res.* **74**, 159–171 (2007).

43. D. M. Mosser, J. P. Edwards, Exploring the full spectrum of macrophage activation. *Nat. Rev. Immunol.* **8**, 958–969 (2008).

44. M. J. Foglia, K. D. Poss, Building and re-building the heart by cardiomyocyte proliferation. *Development* **143**, 729–740 (2016).

45. K. E. Yutzey, Cardiomyocyte proliferation: Teaching an old dogma new tricks. *Circ. Res.* **120**, 627–629 (2017).

46. T. Jackson, M. F. Allard, C. M. Sreenan, L. K. Doss, S. P. Bishop, J. L. Swain, The c-myc proto-oncogene regulates cardiac development in transgenic mice. *Mol. Cell. Biol.* **10**, 3709–3716 (1990).

47. A. Uygur, R. T. Lee, Mechanisms of cardiac regeneration. *Dev. Cell* **36**, 362–374 (2016).

48. R. Karra, K. D. Poss, Redirecting cardiac growth mechanisms for therapeutic regeneration. *J. Clin. Invest.* **127**, 427–436 (2017).

49. N. Kamaly, G. Fredman, M. Subramanian, S. Gadde, A. Pesic, L. Cheung, Z. A. Fayad, R. Langer, I. Tabas, O. C. Farokhzad, Development and in vivo efficacy of targeted polymeric inflammation-resolving nanoparticles. *Proc. Natl. Acad. Sci. U.S.A.* **110**, 6506–6511 (2013).

50. Y. Kharraz, J. Guerra, C. J. Mann, A. L. Serrano, P. Munoz-Canoves, Macrophage plasticity and the role of inflammation in skeletal muscle repair. *Mediators Inflamm.* **2013**, 491497 (2013).

51. S. Lee, H. S. Yun, S. H. Kim, The comparative effects of mesoporous silica nanoparticles and colloidal silica on inflammation and apoptosis. *Biomaterials* **32**, 9434–9443 (2011).

52. N. Koike, D. Fukumura, O. Gralla, P. Au, J. S. Schechner, R. K. Jain, Tissue engineering: Creation of long-lasting blood vessels. *Nature* **428**, 138–139 (2004).

53. Y. D. Lin, C. Y. Luo, Y. N. Hu, M. L. Yeh, Y. C. Hsueh, M. Y. Chang, D. C. Tsai, J. N. Wang, M. J. Tang, E. I. Wei, M. L. Springer, P. C. Hsieh, Instructive nanofiber scaffolds with VEGF create a microenvironment for arteriogenesis and cardiac repair. *Sci. Transl. Med.* **4**, 146ra109 (2012).

54. Y. Li, L. Fan, S. Liu, W. Liu, H. Zhang, T. Zhou, D. Wu, P. Yang, L. Shen, J. Chen, Y. Jin, The promotion of bone regeneration through positive regulation of angiogenic-osteogenic coupling using microRNA-26a. *Biomaterials* **34**, 5048–5058 (2013).

55. Y. Li, L. Fan, J. Hu, L. Zhang, L. Liao, S. Liu, D. Wu, P. Yang, L. Shen, J. Chen, Y. Jin, MiR-26a rescues bone regeneration deficiency of mesenchymal stem cells derived from osteoporotic mice. *Mol. Ther.* **23**, 1349–1357 (2015).

56. X. Zhang, Y. Li, Y. E. Chen, J. Chen, P. X. Ma, Cell-free 3D scaffold with two-stage delivery of miRNA-26a to regenerate critical-sized bone defects. *Nat. Commun.* **7**, 10376 (2016).

57. A. E. Horvai, L. Xu, E. Korzus, G. Brard, D. Kalafus, T. M. Mullen, D. W. Rose, M. G. Rosenfeld, C. K. Glass, Nuclear integration of JAK/STAT and Ras/AP-1 signaling by CBP and p300. *Proc. Natl. Acad. Sci. U.S.A.* **94**, 1074–1079 (1997).

58. H. Ma, R. Guo, L. Yu, Y. Zhang, J. Ren, Aldehyde dehydrogenase 2 (ALDH2) rescues myocardial ischaemia/reperfusion injury: Role of autophagy paradox and toxic aldehyde. *Eur. Heart J.* **32**, 1025–1038 (2011).

59. Y. Li, B. Cai, L. Shen, Y. Dong, Q. Lu, S. Sun, S. Liu, S. Ma, P. X. Ma, J. Chen, MiRNA-29b suppresses tumor growth through simultaneously inhibiting angiogenesis and tumorigenesis by targeting Akt3. *Cancer Lett.* **397**, 111–119 (2017).